First-principles calculations of spatially extended electronic states for nanostructures with a divide-and-conquer method

(

)

28 **12** ( )

Abstract

Linearly scaling methods for the density functional theory (DFT) are powerful tools for the simulation of large systems such as nanostructured materials, biological systems, etc. The existing methods typically focus on the total energy, the electron density, and the forces in the systems. However, evaluation of the electronic state requires a numerically demanding post-processing procedure for these methods.

In this thesis, we present an efficient post-processing method for the electronic state calculation of general materials based on the divide-and-conquer (DC) DFT, which is one of the linear scaling algorithm for DFT. In DC-DFT, a huge system is divided into small fragments and the electron density of the total system is obtained by patching the fragment densities. To calculate the electronic state, we reuse the fragment orbitals used for this density evaluation. We first organize a basis set by clipping the core domain of the fragment orbitals. Eliminating redundant information, we can further reduce the basis set size. The Kohn-Sham Hamiltonian matrix defined with the basis set is constructed simply by calculating the inner products among the orbitals in the neighboring fragments. As a result, the present method yields fast and accurate description of the orbital energies and the orbital wave functions of general large systems. Remarkably, our scheme enables us to implement an efficient algorithm for the calculation with the exact exchange.

We analyze the parameter dependence of our method, which gives us a guide for proper selection of the parameters in applications. We also perform benchmark tests to show that our method can substantially reduce the computational cost with reasonable accuracy. In our method, the number of the basis functions per atom becomes roughly 4–10 depending on configurations of the fragments.

We present computational results of our method for P-doped Si, P-doped Ge and In-GaN/GaN super-lattice systems. In these results, we show that our scheme can represent wave functions delocalized in the total system.

Acknowledgments

Contents

Chapter 1

Introduction

1.1 First-principles simulations for large systems

First principles calculations based on the density functional theory (DFT) [1, 2] have been widely used for investigating material properties and phenomena in condensed matter physics. While calculations with hundreds of atoms are currently routine, there is a demand for simulations of larger systems. However, the computational cost of the conventional DFT calculations rapidly grows as the order of N cubed, where N is the number of atoms contained in a target system. Thus the first principles calculations for large systems require massive computational effort which is often impossible to realize. This problem was a motivation to develop the linear-scaling or $O(N)$ methods [3, 4], whose computational cost increase moderately as the order of N.

Let us start with an overview for the computational cost of the standard DFT calculations. In Kohn-Sham DFT, which will be reviewed in Sec. 2.1, a problem for many interacting electrons is mapped into a set of effective Schrödinger equations for single-electron, called Kohn-Sham equations. The main contribution to the computational time is that for the diagonalization of these equations. We shall see how the diagonalization cost grows with system size for each class of basis set [3].

1.1.1 Plane-wave basis set

The plane-wave basis set is most widely used in the DFT calculations. Let us consider a target system with a large periodic unit cell. Each orbital wavefunction $\psi_i(\mathbf{r})$, an eigenvector of the Kohn-Sham equation, is expanded as follows:

$$\psi_i(\mathbf{r}) = \sum_{|\mathbf{G}| < G_{\max}} c_i(\mathbf{G}) \exp(i\mathbf{G} \cdot \mathbf{r}), \tag{1.1}$$

where i is the band index and $\mathbf{G}$ is the reciprocal lattice vector for the unit cell. $G_{\max}$ is a cutoff parameter restricting the number of the reciprocal lattice vectors N_G. Here we omitted the wave number $\mathbf{k}$ since the Brillouin zone is small for the large system.

7

The eigenvalue problem of the equations is solved by the iterative method such as the conjugate gradient method. The orbital wavefunctions for the valence electrons are only required to evaluate the electron density $\rho(\mathbf{r})$, the key component of DFT (see Sec. 2.1):

$$\rho(\mathbf{r}) = \sum_{i}^{\text{occ}} |\psi_i(\mathbf{r})|^2, \tag{1.2}$$

where the sum is only taken over the valence electrons. Thus the number of the wavefunctions to be solved, N_{band}, is slightly larger than that of the valence electrons. Generally, N_{band} is roughly 100 times smaller than N_G.

There are two computationally expensive parts: the calculation of the density Eq. (1.2) and the orthonormalization of the orbitals. The computational cost of the former becomes $O(N_{\text{band}}N_G\log(N_G))$, where $N_G\log(N_G)$ comes from the fast Fourier transformation (FFT) for each orbital: $c_i(\mathbf{G}) \rightarrow \psi_i(\mathbf{r})$. The cost for the latter is $O(N_{\text{band}}^2 N_G)$ since the calculation includes the inner-product operation for all pairs of index i. For large systems, the former becomes a significant bottleneck due to the inefficiency of FFT for parallel computation, and the latter becomes the most expensive part with $O(N_{\text{band}}^2 N_G) = O(N^3)$ cost.

The main advantages of the plane-wave basis set are accuracy and universality thanks to its apparent completeness. The accuracy can be improved systematically with increasing one parameter, G_{max}. Additionally, the basis set can be easily applied to general condensed matter because it is independent of properties or positions of atoms.

1.1.2   Real-space basis set

The real-space basis set can be classified roughly into two types. The real-space grid, or finite difference method [5–7], represents the orbitals on the grid-point basis set $\{|\mathbf{r}\rangle\}$. The kinetic term in the Kohn-Sham equation is practically represented as the finite differences such as,

$$\frac{\partial^2}{\partial x^2}\psi(x, y, z) \approx \sum_{m=-M}^{M} C_m\psi(x + mh, y, z), \tag{1.3}$$

where h is the grid spacing and M is the order of the expansion. C_m means the coefficient of the finite difference. The parameters controlling the accuracy are h and M, which play a similar role of G_{max}. As the plane wave case, the accuracy can be improved systematically with these parameters.

The other real-space basis set is the local real-space basis set such as the finite element [8], the wavelet [9], the Lagrange functions [10], etc. In these methods, the orbitals are expanded with spatially localized functions. The size of the basis set is generally smaller than N_G but larger than that of the atomic-like basis set referred to in the next subsection.

In both cases, the sparsity of the Hamiltonian matrix thanks to the locality of the basis set yields efficient parallelization. Moreover, the density evaluation does not require FFT for the orbitals since the orbitals are expressed in the real space. In the finite differences method, the Poisson equation for the Hartree potential can be solved by the multi-grid method [11] without FFT for the density. Nonetheless, the $O(N^3)$ orthonormalization for the orbitals is needed as the plane-wave case.

1.1.3 Atomic-like basis set

The atomic-like basis set is categorized into the numerical atomic orbitals [12] for all-electron calculations and the pseudo-atomic orbitals [13] for calculations with pseudopotentials. These basis functions mimic the wavefunctions of atoms:

$$\chi_{nlm}(\mathbf{r}) = R_{nl}(\mathbf{r})Y_{lm}(\hat{\mathbf{r}}), \tag{1.4}$$

where $R_{nl}(\mathbf{r})$ and $Y_{lm}(\hat{\mathbf{r}})$ are a radial function and a spherical harmonic, respectively. This expression enables analytic inner-product operations for the spherical part, which facilitate the calculation of the Hamiltonian and the overlap matrix.

The main advantages of the basis set is its locality and relatively small size of the basis set. With the former advantage, the cost for the construction of the Hamiltonian matrix is $O(N)$ thanks to the sparsity of the matrix. The orthonormalization cost is $O(N_{\text{band}}^2 N_{\text{basis}})$, where the number of the basis functions N_{basis} is far smaller than N_G.

The disadvantage of the basis set is the unsystematic nature of its convergence. There are neither clear rule for how to increase their radial and angular freedom nor comprehensible parameter such as G_{max} which controls the accuracy.

1.2 Linear scaling methods

The various linear-scaling, or $O(N)$ methods have been proposed to overcome the problem of the computational cost [3,4]. These methods avoid the time-consuming diagonalization for global electronic states and evaluate the electron density without such wavefunctions.

The majority of $O(N)$ methods rely on the sparsity of the density matrix. Here, the density matrix is defined with $\psi_i(\mathbf{r})$ as

$$\rho(\mathbf{r}, \mathbf{r}') = \sum_i^{\text{occ}} \psi_i(\mathbf{r})\psi_i^*(\mathbf{r}'). \tag{1.5}$$

The electron density can be obtained as $\mathbf{r} = \mathbf{r}'$. The density matrix is localized in broad classes of systems [14–16]. For $T = 0$ insulators and $T > 0$ metals, the density matrix exponentially decays:

$$\rho(\mathbf{r}, \mathbf{r}') \sim \exp(-\gamma|\mathbf{r} - \mathbf{r}'|), \quad |\mathbf{r} - \mathbf{r}'| \longrightarrow \infty. \tag{1.6}$$

For $T = 0$ metals, the decay obeys a power low. With localized basis functions $\{\chi_i(\mathbf{r})\}$ such as the atomic-like or the local real-space basis set, the density matrix can be represented with a sparse matrix $\{K_{ij}\}$:

$$\rho(\mathbf{r}, \mathbf{r}') = \sum_{ij} \chi_i(\mathbf{r}) K_{ij} \chi_j(\mathbf{r}'). \tag{1.7}$$

There are several methods for obtaining the sparse density matrix with $O(N)$ cost (for detailed review, see [3,4,12]).

The other group of $O(N)$ methods evaluate the electron density through the Green's function $\hat{G}(E) = (E - \hat{H})^{-1}$,

$$\rho(\mathbf{r}) = \oint_C \frac{dE}{2\pi i} \langle \mathbf{r}|\hat{G}(E)|\mathbf{r}\rangle, \qquad (1.8)$$

where C is a contour in the complex-energy plane enclosing the eigenenergies of the valence states. The wavefunctions do not appear in this expression of $\rho(\mathbf{r})$. The Krylov subspace method [17–21] utilizes the atomic-like basis set and the Lanczos or Arnoldi iteration for the Kohn-Sham Hamiltonian matrix to calculate the Green's function. The method of Ref. [22] uses the orbitals of overlapping subsystems as the basis functions to calculate the Green's function. The contour integral of Eq. (1.8) can be calculated with $O(N)$ cost.

The simplest and most intuitive approach is the divide-and-conquer approach to density functional theory (DC-DFT) [20, 23–31]. In DC-DFT, the whole system is divided into overlapping subsystems, which we call fragments. The total energy is minimized by an iterative procedure of two steps: (i) Solving the Kohn-Sham equation for each fragment separately, and (ii) gathering the electron densities of the fragments to evaluate the Kohn-Sham potential. DC-DFT utilizes neither the density matrix nor the Green's function and relies only on the nearsighted principle of the electron density (Sec. 2.2.1). The time-consuming calculations such as FFT of the orbitals in the plane-wave case are simply done within each fragment, so that the computational cost becomes $O(N)$.

DC-DFT has attractive characters such as robust convergence properties and ease of implementation. Especially, DC-DFT allows us to use broad classes of the basis set including the plane-wave basis set [28, 29, 31]. DC-DFT with the plane-wave basis set is highly attractive because this approach can establish both the $O(N)$ cost and the mature handling of the plane-wave basis set. The plane-wave DC-DFT has high accuracy and universality stemming from the plane wave. For these reasons, we focus only on this method in the present thesis.

1.3 Electronic state calculation with linear scaling methods

As seen above, $O(N)$ methods avoid the diagonalization for the electronic state to achieve the $O(N)$ cost. However, this becomes an obstacle for direct access to quantities or properties related with the electronic state such as the density of states. There is interest in the electronic state calculation for large systems. Generally, the electronic state calculation is needed to investigate properties related with the density of states, a mechanism of the chemical reactions, etc. For example, with their $O(N^3)$ finite difference code [32], Ref. [33] investigated the twisted bilayer graphene with various twist angles, where the largest cell consists of 22708 atoms. They found a localization of the Dirac electrons below a critical twist angle and an interesting behavior of the Fermi velocity with respect to the twist angle, and these analyses require the orbital wavefunctions of the entire systems.

Thus it is important to evaluate the electronic state whose properties crucially relies on the hugeness of systems. This goal can be achieved if we can accelerate the $O(N^3)$ diagonalization step on the basis of the $O(N)$ method.

The diagonalization for the total system needs a very large basis set and a numerically demanding computation for the Hamiltonian matrix elements. With the former problem, there is a method for constructing a small basis set from the atomic-like basis functions [34, 35]. The latter problem originates from the explicit treatment of the Hamiltonian operator in the matrix-elements calculations. For DC-DFT, this computation seems redundant since the Kohn-Sham Hamiltonian for each overlapping fragment has already been diagonalized in the DC-DFT calculation. Namely, in principle, the orbitals of the fragments contain information of the total Hamiltonian. We desire a post-processing method for adopting the fragment orbitals to accelerate the Hamiltonian diagonalization for the total system.

Here we see a successful example in a previous study. The fragment molecular orbital (FMO) method [36] is a particular DC method specialized for biological molecules (for details, see Sec. 2.2.4). There are several post-processing methods of FMO to compute the electronic state of the whole molecule by using information of the fragments [37–41]. In particular, the FMO linear combination of molecular orbitals (LCMO) method [40, 41] is a highly efficient method. In this post-processing method, the one-electron Hamiltonian matrix is constructed by utilizing the molecular orbitals of the fragments as basis functions. Each molecular orbital of the total molecule is expressed as an LCMO of the fragments without the redundant recalculation. This method can reduce the basis set size and the computational cost for calculating the matrix elements. However, this method cannot be applied to general materials straightforwardly because FMO essentially relies on the specific features of the sp^3 orbitals of carbon atoms.

1.4   Purpose of the study and outline of the thesis

The purpose of our study is to develop a new post-processing method of DC-DFT, which enables us to calculate the electronic state for general materials by using the fragment orbitals derived from the DC-DFT calculation. To this end, we use DC-DFT with plane-wave basis set, especially the lean divide-and-conquer (LDC) DFT [31], that can be applied to general materials with a systematic procedure. In our method, a small number of basis functions are constructed by reducing the fragment orbitals. The total Hamiltonian matrix defined by the localized basis set is calculated easily from the fragment orbitals and their orbital energies in the manner of FMO-LCMO. Each wave function of the whole system is represented by a linear combination of the fragment orbitals (LCFO). The diagonalization process can be performed with little computational cost thanks to the reduced number of the basis functions. Thus our procedure, called DC-LCFO hereafter, has advantages of a low cost and versatility.

This thesis is organized as follows. Chapter 2 outlines DFT and DC-DFT. Chapter 3 describes a formulation and implementation of our DC-LCFO. In chapter 4, we analyze the parameter dependence for results of our method and the feasibility of the matrix-size

reduction of the Hamiltonian. Chapter 5 presents examples of application. We compare the eigenenergies and the wave functions with those of the conventional method in P-doped Si, P-doped Ge, and InGaN/GaN superlattice systems. Finally, conclusion is given in Chapter 6. In appendix A, we compare the formulation of DC-LCFO with that of FMO-LCMO. Appendix B describes an extension of our method for calculating the electronic state with the k-point sampling.

Table 1.1: List of acronyms used in this thesis.

Acronym	Meaning
DFT	Density Functional Theory
KS	Kohn Sham
DC	Divide and Conquer
DC-DFT	DC approach to DFT
LDC-DFT	Lean Divide-and-Conquer DFT
DC-LCFO	DC Linear Combination of Fragment Orbitals
RMS	Root Mean Square
MAE	Maximum Absolute Error
FMO	Fragment Molecular Orbital
FMO-LCMO	FMO Linear Combination of Molecular Orbitals
LS3DF	Linearly Scaling 3 Dimensional Fragment

Chapter 2

Density functional theory and divide-and-conquer method

2.1 Density functional theory

We first review the density functional theory (DFT) [1,2]. The statement of the Hohenberg-Kohn Theorem is as follows: If N interacting electrons move in an external potential $V_{\text{ext}}(\mathbf{r})$, the electron density of the ground state minimizes the functional,

$$E[\rho] = F[\rho] + \int d^3 r V_{\text{ext}}(\mathbf{r})\rho(\mathbf{r}), \tag{2.1}$$

where $F[\rho]$ is a universal functional of the electron density $\rho(\mathbf{r})$ and the minimum value of the functional $E[\rho]$ is equal to the exact ground-state energy of the electrons. Moreover, such electron density is uniquely determined.

Kohn and Sham established a practical scheme for calculating the ground state density [2]. They defined the functional $E[\rho]$ as

$$E[\rho] = T[\rho] + \int d^3 r V_{\text{ext}}(\mathbf{r})\rho(\mathbf{r}) + \frac{1}{2} \int d^3 r \int d^3 r' \frac{\rho(\mathbf{r})\rho(\mathbf{r}')}{|\mathbf{r} - \mathbf{r}'|} + E_{\text{xc}}[\rho], \tag{2.2}$$

where $T[\rho]$ is the kinetic energy of virtual non-interacting electrons,

$$T[\rho] = \sum_{i=1}^{N} \int d^3 r \psi_i^*(\mathbf{r}) \left(-\frac{1}{2}\nabla^2\right) \psi_i(\mathbf{r}), \tag{2.3}$$

and the density distribution is identical to that of the non-interacting electrons,

$$\rho(\mathbf{r}) = \sum_{i=1}^{N} |\psi_i(\mathbf{r})|^2. \tag{2.4}$$

The equation for $\psi_i(\mathbf{r})$, called Kohn-Sham (KS) equation, is derived from the minimization condition $\delta E[\rho]/\delta \psi_i^*(\mathbf{r}) = 0$,

$$\left[-\frac{1}{2}\nabla^2 + \hat{V}_{\text{KS}}[\rho]\right]\psi_i(\mathbf{r}) = \varepsilon_i \psi_i(\mathbf{r}), \tag{2.5}$$

where the energy eigenvalue ε_i originates from the Lagrange multiplier corresponding to the orthonormal condition of $\{\psi_i\}$. Here, the KS potential $\hat{V}_{KS}[\rho]$ is defined as follows:

$$
\begin{aligned}
\hat{V}_{KS}[\rho] &\equiv \frac{\delta}{\delta\rho(\mathbf{r})}\left[\int d^3r V_{ext}(\mathbf{r})\rho(\mathbf{r}) + \frac{1}{2}\int d^3r \int d^3r' \frac{\rho(\mathbf{r})\rho(\mathbf{r}')}{|\mathbf{r}-\mathbf{r}'|} + E_{xc}[\rho]\right] \\
&= V_{ext}(\hat{\mathbf{r}}) + V_H(\hat{\mathbf{r}}) + V_{xc}(\hat{\mathbf{r}}).
\end{aligned}
\tag{2.6}
$$

Eq. (2.5) is the Schrödinger-like equation but the potential $\hat{V}_{KS}[\rho]$ depends on the density $\rho(\mathbf{r})$. Therefore it is necessary to iteratively solve Eq. (2.5) in the self consistent manner.

The exchange-correlation functional $E_{xc}[\rho]$ is the difference between the functional of the interacting electrons and that of the virtual non-interacting electrons for the kinetic energy plus the electron-electron interaction. However, the exact formula of $E_{xc}[\rho]$ has been unknown.

A reasonable approximation is that the functional $E_{xc}[\rho]$ depends solely upon the value of the electron density at each point (local density approximations, or LDA [2,42]). In the LDA, the functional form of $E_{xc}[\rho]$ is derived from that of the homogeneous electron gas. The generalized gradient approximations (GGA) are variants of the LDA that include the gradient of the density in order to account for the non-homogeneity of the electron density. In the present paper, we mostly employ the PBE functional [43], which is a kind of the GGA functionals.

The hybrid functionals are more sophisticated schemes which represent $E_{xc}[\rho]$ as a hybrid of the LDA (or GGA) and the Hartree-Fock approximation. For example, the PBE0 hybrid functional [44] is given as follows:

$$
E_{xc}^{PBE0} = \frac{1}{4}E_x^{HF} + \frac{3}{4}E_x^{PBE} + E_c^{PBE},
\tag{2.7}
$$

where E_x^{PBE} and E_c^{PBE} are the exchange part and the correlation part of the GGA-PBE functional, respectively, and E_x^{HF} is the exact exchange energy functional,

$$
E_x^{HF} = -\frac{1}{2}\sum_{i,j=1}^{N}\int d^3r \int d^3r' \frac{\psi_i^*(\mathbf{r})\psi_j^*(\mathbf{r}')\psi_i(\mathbf{r}')\psi_j(\mathbf{r})}{|\mathbf{r}-\mathbf{r}'|}.
\tag{2.8}
$$

The exact (or Hartree-Fock) exchange potential operator is given by

$$
[\hat{V}_x^{HF}\psi_i](\mathbf{r}) = \frac{\delta E_x^{HF}}{\delta\psi_i^*(\mathbf{r})} = -\sum_{j=1}^{N}\psi_j(\mathbf{r})\int d^3r' \frac{\psi_j^*(\mathbf{r}')\psi_i(\mathbf{r}')}{|\mathbf{r}-\mathbf{r}'|}.
\tag{2.9}
$$

In the above formulations, we discussed only the $T=0$ case. For general cases [45], the occupation of the electrons is determined by the chemical potential μ, such as

$$
\rho(\mathbf{r}) = \sum_i f(\varepsilon_i - \mu)|\psi_i(\mathbf{r})|^2,
\tag{2.10}
$$

where f is the Fermi-Dirac distribution function.
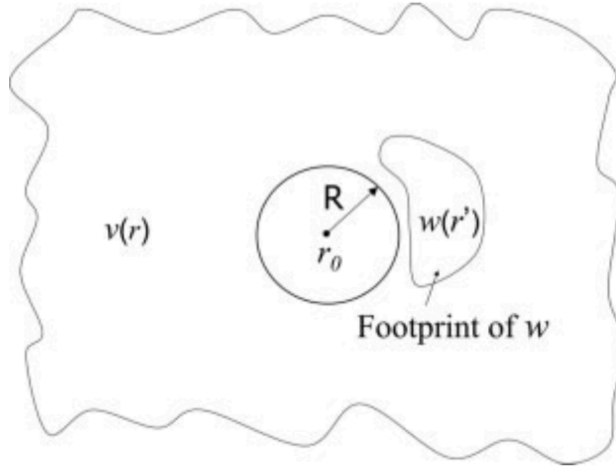
Figure 2.1: Schematic of the nearsightedness principle. $v(r)$ (= $V_{\text{ext}}(\mathbf{r})$ in the text) is the unperturbed external potential, $w(r)$ (= $\Delta V(\mathbf{r})$ in the text) is the perturbing potential outside a sphere of radius R, which is centered on the point of interest $\mathbf{r}_0$. "footprint" means to a region that $w(r)$ has a nonzero value. Reprinted the figure from Ref. [46]. Copyright (2005) by the National Academy of Sciences.

2.2 Divide-and-conquer approach to density functional theory

2.2.1 Quantum nearsightedness

The nearsightedness principle explains why O(N) methods can exist. The concept of nearsightedness of electronic matter (NEM) has been established by W. Kohn and E. Prodan [46, 47], where "electronic matter" means a system of many interacting electrons in the thermal equilibrium in an external potential $V_{\text{ext}}(\mathbf{r})$. Let us consider the change of the electron density $\rho(\mathbf{r}_0)$ at a point $\mathbf{r}_0$ under the action of a potential perturbation $\Delta V(\mathbf{r})$, which vanishes inside a sphere of radius R centered at $\mathbf{r}_0$ (see Fig. 2.1). We also assume that the chemical potential μ is held fixed in this perturbation. NEM is a statement that the density change $\Delta\rho(\mathbf{r}_0)$ at $\mathbf{r}_0$ due to $\Delta V(\mathbf{r})$ is bounded by a maximum magnitude $\overline{\Delta\rho}$, which decays monotonically as a function of R,

$$\Delta\rho(\mathbf{r}_0) \leq \overline{\Delta\rho}(\mathbf{r}_0; R) \longrightarrow 0 \quad (R \longrightarrow \infty), \tag{2.11}$$

for broad classes of systems. Prodan and Kohn showed that the decay follows power lows in ordered gapless systems, while the decay is exponential in ordered gapped systems and disordered systems [46]. For a given $\mathbf{r}_0$ and $\Delta\rho$, we can solve for R in $\overline{\Delta\rho}(\mathbf{r}_0; R) = \Delta\rho$ and define the "nearsightedness range" $R(\mathbf{r}_0; \Delta\rho)$. With any perturbation $\Delta V(\mathbf{r})$ beyond the distance $R(\mathbf{r}_0; \Delta\rho)$, the density change at $\mathbf{r}_0$ cannot exceed $\Delta\rho$.

NEM implies the possibility of the linearly scaling methods. To evaluate the electron density within a certain region, it is possible to separate a subsystem with a sufficiently
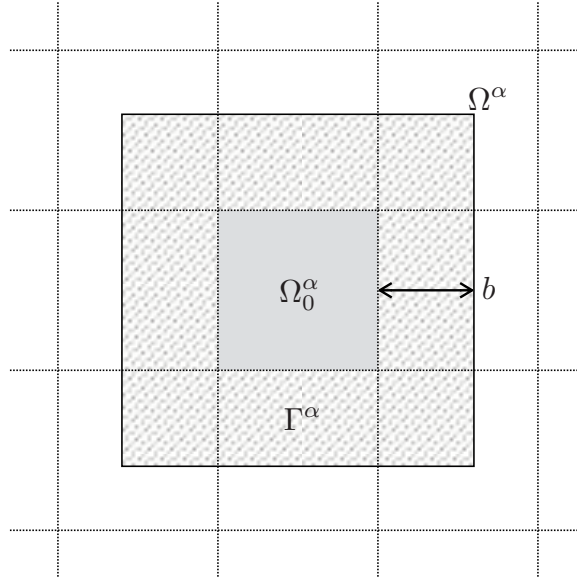
Figure 2.2: Schematic 2D image of the DC algorithm. The whole system Ω is represented as a union of non-overlapping core domains $\{\Omega_0^\alpha\}$. Physical quantities of Ω_0^α are evaluated on the fragment $\Omega^\alpha = \Omega_0^\alpha \bigcup \Gamma^\alpha$, where Γ^α is a buffer layer whose thickness is b.

large buffer zone, since the electron density cannot feel any potential perturbation beyond $R(\mathbf{r}; \Delta\rho)$ within an accuracy $\Delta\rho$. Thus we can divide a system into subsystems and obtain the total electron density by summing those of the subsystems calculated separately. This is the physical basis of linearly scaling methods, called the divide-and-conquer methods.

2.2.2 Divide-and-conquer method

As explained in Sec. 1.1, the computational cost of the DFT calculation grows rapidly with system size. Nonetheless, the nearsightedness principle enables the linear scaling of the computational cost. We shall consider a large system enclosed in a physical space Ω. Let us represent Ω as a union of non-overlapping core domains, $\Omega = \bigcup_\alpha \Omega_0^\alpha$, where $\Omega_0^\alpha \bigcap \Omega_0^\beta = \emptyset \, (\alpha \neq \beta)$. With the nearsightedness principle, the electron density in each core domain can be approximately evaluated from a calculation for a subsystem, called a fragment, $\Omega^\alpha = \Omega_0^\alpha \bigcup \Gamma^\alpha$, where Γ^α is the buffer zone surrounding Ω_0^α (Fig. 2.2). Ideally, the thickness b of Γ^α is dictated by the nearsightedness range $R(\mathbf{r}; \Delta\rho)$ for an intended accuracy $\Delta\rho$: b is chosen so that $\Delta\rho(\mathbf{r}) \leq \Delta\rho$, where $\mathbf{r}$ is any point on the boundary of Ω_0^α and $\Delta\rho(\mathbf{r})$ is the error due to the artificial boundary of the fragment. In reality, this b determination requires prior knowledge of a target system, and therefore b is usually chosen by heuristics. The above approach for DFT is called the divide-and-conquer approach to density functional theory (DC-DFT) [20, 23–31]. We now review the detailed formalism of this approach.

16

In DC-DFT, the electron density of the entire system (total density) is represented as the sum of those for Ω_0^α:

$$\rho(\mathbf{r}) = \sum_\alpha \bar{\rho}^\alpha(\mathbf{r}), \quad \rho^\alpha(\mathbf{r}) = \sum_i f(\varepsilon_i^\alpha - \mu)|\phi_i^\alpha(\mathbf{r})|^2, \tag{2.12}$$

where $\phi_i^\alpha(\mathbf{r})$ and ε_i^α are the orbital wave function of the α-th fragment and corresponding orbital energy, respectively, and $\bar{\rho}^\alpha(\mathbf{r})$ is the density in the core domain Ω_0^α clipped from the density of the fragment $\rho^\alpha(\mathbf{r})$:

$$\bar{\rho}^\alpha(\mathbf{r}) = \begin{cases} \rho^\alpha(\mathbf{r}) & (\mathbf{r} \in \Omega_0^\alpha) \\ 0 & (\mathbf{r} \notin \Omega_0^\alpha) \end{cases}. \tag{2.13}$$

The chemical potential μ in Eq. (2.12) must be fixed as that of the total system, and therefore μ is determined by the electron number condition of the whole system,

$$N = \int d^3 r \rho(\mathbf{r}). \tag{2.14}$$

The orbital wave functions $\{\phi_i^\alpha(\mathbf{r}), \mathbf{r} \in \Omega^\alpha\}$ and corresponding orbital energies $\{\varepsilon_i^\alpha\}$ for each fragment are derived from the Kohn-Sham (KS) equation for the fragment,

$$\hat{H}^\alpha|\phi_i^\alpha\rangle \equiv \left[-\frac{1}{2}\nabla^2 + \hat{V}_{KS} + \hat{v}_{bc}^\alpha \right]|\phi_i^\alpha\rangle = \varepsilon_i^\alpha|\phi_i^\alpha\rangle, \tag{2.15}$$

where $\hat{V}_{KS} = \hat{V}_{KS}[\rho]$ is the KS potential with the total density and $v_{bc}^\alpha(\mathbf{r})$ is the boundary potential representing effects of the artificial fragment boundary $\partial\Omega^\alpha$.

The fragment orbitals $\{\phi_i^\alpha(\mathbf{r})\}$ are locally orthonormal:

$$\int_{\Omega^\alpha} d^3 r \phi_i^{\alpha*}(\mathbf{r})\phi_{i'}^\alpha(\mathbf{r}) = \delta_{ii'}. \tag{2.16}$$

The boundary conditions of $\{\phi_i^\alpha(\mathbf{r})\}$ at the fragment boundary $\partial\Omega^\alpha$ will be discussed in Sec. 2.2.3.

The minimization of the total energy $E[\rho]$ with respect to $\{\phi_i^\alpha(\mathbf{r})\}$ is performed through the following iterative procedure:

(1) Calculate the KS potential $\hat{V}_{KS}[\rho]$ using the total density of the previous step or the initial value (for first iteration). Especially, the Hartree potential, representing the long-range electrostatic influence, is derived from the global Poisson equation.

(2) Solve the fragment KS equations independently.

(3) Aggregate the fragment densities obtained by the fragment orbitals to calculate the total density.

(4) Determine the chemical potential μ so that $N = \int d^3 r \rho(\mathbf{r})$, where N is the number of the valence electrons.

(5) Calculate the new total density $\rho(\mathbf{r})$.

In the step 1 (or the step 5), it is required to update the potential (density) by the potential-mixing (charge-mixing) scheme.

The computational cost for this procedure is linear scaling with the system size. To minimize the cost, the edge size of each "cubic" core region (which we call a) is chosen as follows: The total time of the computation T_{total} is given by $N_{\text{fragment}} \cdot T_{\text{fragment}}$, where $N_{\text{fragment}} =$(volume of Ω)$/a^d$ is the number of the fragments in d-dimension. The time of the electronic structure calculation for each fragment T_{fragment} is proportional to $(a + 2b)^{d\nu}$, where ν is the order of the calculation (=2–3 for DFT) and the buffer thickness b is fixed as the nearsightedness range. Thus,

$$T_{\text{total}} = N_{\text{fragment}} \cdot T_{\text{fragment}} \propto \frac{1}{a^d}(a + 2b)^{d\nu}. \tag{2.17}$$

Differentiating T_{total} with a, we obtain the optimized edge length of the core domain,

$$a = \frac{2b}{\nu - 1}. \tag{2.18}$$

For DC-DFT, this indicates the edge length of each core domain Ω_0^α is assume as the same or twice the buffer thickness b. If the hybrid functionals were used, more small a is required for the cost of the DC calculation since ν is higher than 3. Nonetheless, we put $a = b$ even in this case because the Hamiltonian matrix of our method becomes sparse with such a (see Sec. 3.3).

Note that we clipped the density of Ω_0^α with the step wise manner in Eq. (2.13), while many DC-DFT papers utilized the continuous weight function,

$$\sum_\alpha p^\alpha(\mathbf{r}) = 1, \tag{2.19}$$

for the density summation:

$$\rho(\mathbf{r}) = \sum_\alpha p^\alpha(\mathbf{r})\rho^\alpha(\mathbf{r}). \tag{2.20}$$

However, these weight functions $\{p^\alpha(\mathbf{r})\}$ induce difficulty for the Hamiltonian reconstruction in our method. Namely, if the basis functions of our method (will be discussed in Sec. 3.2) were defined by using the clipping with $\{p^\alpha(\mathbf{r})\}$, an overlap matrix of the basis functions should be required to diagonalize the total Hamiltonian, because the basis functions of the respective fragments overlap each other. Thus we simply utilize the step wise projection as Eq. (2.13).

2.2.3 Fragment boundaries

We shall discuss about the boundary conditions of $\{\phi_i^\alpha(\mathbf{r})\}$ at the fragment boundary $\partial\Omega^\alpha$. The most often used conditions are the "hard wall" boundary conditions, which restrict the fragment orbitals as $\phi_i^\alpha(\mathbf{r}) = 0$ ($\mathbf{r} \in \partial\Omega^\alpha$). The boundary potential $v_{\text{bc}}^\alpha(\mathbf{r})$ corresponding to the hard wall is given by,

$$v_{\text{bc}}^\alpha(\mathbf{r}) = \begin{cases} 0 & (\mathbf{r} \in \Omega^\alpha) \\ \infty & (\mathbf{r} \notin \Omega^\alpha) \end{cases}. \tag{2.21}$$

The basis set suitable for the hard wall conditions is the atomic-like basis [20, 24, 26] or the real-space basis such as the real-space grid basis (finite differences method) [27, 30] or the Lagrange basis [22].

The periodic boundary conditions are another choice, which correspond to the Γ-point ($\mathbf{k} = 0$ point) calculations with the unit cell Ω^α. These conditions enable us to utilize the plane-wave basis for the calculation of the fragments [28, 29, 31]. In the present thesis, we use the plane-wave basis in all the calculations.

We note another aspect of the boundary potential $v_{bc}^\alpha(\mathbf{r})$. Ref. [30] introduced the "density-template" potential defined as

$$v_{bc}^\alpha(\mathbf{r}) = \frac{\rho^\alpha(\mathbf{r}) - \rho(\mathbf{r})}{\xi}, \tag{2.22}$$

where $\xi > 0$ is an adjustable parameter. This potential reduces the discrepancy $\Delta\rho^\alpha(\mathbf{r}) = \rho^\alpha(\mathbf{r}) - \rho(\mathbf{r})$ at the boundary, and therefore brings about the fast convergence in the SCF iteration. LDC-DFT [31] applied the plane-wave basis and the density-template potential for the fragments.

2.2.4 Related methods

Here we refer to the methods related to DC-DFT which appear in this thesis. The fragment molecular orbital (FMO) method [36] is one of the DC methods specialized for biological molecules such as proteins. The difference between FMO and conventional DC-DFT is that FMO utilizes two types of the fragments: small pieces of a whole molecule (monomers) and the unions of two monomers (dimers). Sometimes the unions of three monomers (trimers) are also used for more precise calculations. Fig. 2.3 shows the example of the fragmentation for chignolin molecule [41]. In FMO, the total energy E of the whole molecule is obtained by patching the monomer energies $\{E_I\}$ and the inter-monomer energies across two monomers that given with the dimer energies $\{E_{IJ}\}$:

$$E = \sum_I E_I + \sum_{I>J} (E_{IJ} - E_I - E_J), \tag{2.23}$$

where I and J are the monomer indices. The last two terms in the parenthesis cancel the double-counting terms. The summation form of Eq. (2.23) is the basic idea for the Hamiltonian expansion of FMO-LCMO.

The boundary of the fragments is cut with a projection of the carbon sp^3 orbitals to purify dangling bonds. Hence the boundary conditions or the boundary potential $v_{bc}^\alpha(\mathbf{r})$ of the fragments cannot be described straightforwardly.

The linearly-scaling 3-dimensional fragment (LS3DF) method [28,29] is closely rerated with FMO, but can be applied to large semiconductor systems. As FMO, this method utilizes several types of differently sized fragments. In 2D systems, for simplicity, 4 kinds of fragments are defined as Fig. 2.4: small square pieces (1×1); two types of rectangular pieces (1×2, 2×1); large square pieces (2×2). Generally 2^d kinds of fragments are

used in d-dimensional systems. The total electron density is evaluated by summing up the fragment densities with differing signs:

$$\rho(\mathbf{r}) = \sum_F \alpha_F \rho_F(\mathbf{r}), \tag{2.24}$$

where F is a fragment index and α_F is a sign factor: $\alpha_F = +$ for 1×1 and 2×2, $= -$ for 1×2 and 2×1. We note that effects from the buffer regions are canceled out between the different types of fragments, so that the clipping of the core domain as Eq. (2.13) is not required. The fragment boundary is imposed the periodic boundary conditions, however, with an artificial vacuum layer inserted into the buffer region. The dangling bonds at the artificial surface of the fragments are passivated with the pseudo-Hydrogen atoms. The summation formula Eq. (2.24) will be related to the Hamiltonian reconstruction of our method (see Appendix A).
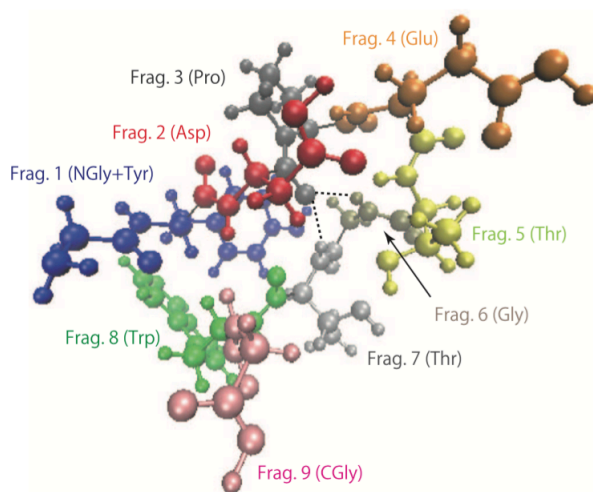
Figure 2.3: A schematic of the FMO fragmentation for chignolin molecule with the monomer indices. Reprinted the figure from Ref. [41]. Copyright (2013) by the American Institute of Physics.
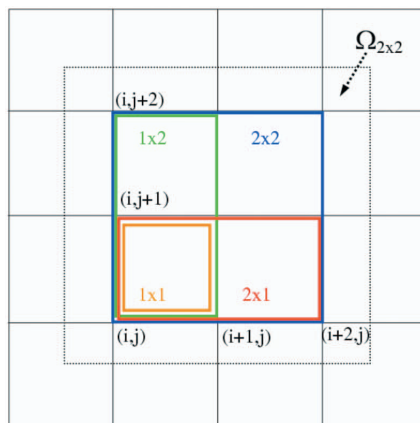
Figure 2.4: A schematic 2D view of the LS3DF fragments. The dashed line denotes the area of the 2×2 fragment with the buffer region. Reprinted the figure from Ref. [28]. Copyright (2008) by the American Physical Society.

Chapter 3

Formalism

3.1 Strategy

Here we briefly describe our strategy and basic ideas to develop a versatile method, dubbed as DC-LCFO (Ref: Yamada *et al.* [48]). There are several methods for DC-DFT with different basis functions and different ways of handling the boundary effects of the fragments: their accuracy depends on the target systems. In the present thesis, we adopt LDC-DFT [31] as the basis, which utilizes the density template potential [30] as $v_{bc}^{\alpha}(\mathbf{r})$ and the periodic boundary conditions at $\partial\Omega^{\alpha}$ on the fragment KS orbitals. This method is suitable for calculations of condensed matter since it has relatively small overhead and convenient buffer configurations for calculations (see Sec. 3.3). Note that we use the step-wise projection in Eq. (2.12) for simplicity [30], though continuous weight functions are used in the original LDC-DFT paper.

Our fundamental assumption is that the eigenstates near the Fermi level can be well represented by patching a small number of fragment orbitals in the corresponding energy region [40, 41]. Thereby we shall first develop an algorithm to generate basis functions from the fragment orbitals $\{\phi_i^{\alpha}\}$ within the low-energy region.

As the next step, we shall introduce a method to construct the total Hamiltonian matrix using the basis functions and the fragment Hamiltonians $\{\hat{H}^{\alpha}\}$ defined in Eq. (2.15). The matrix elements of the Hamiltonian can be constructed simply by inner products among the fragment orbitals. Hence the Hamiltonian matrix can be obtained without time-consuming calculations even when the exact exchange potential is taken into account.

The resultant basis functions are defined on each core domain Ω_0^{α} and therefore it is not necessary to consider the total overlap matrix of the whole system. Moreover, the Hamiltonian matrix has a far smaller dimension than the plane-wave basis case because the new basis functions are made of the fragment orbitals in the low-energy region. Notably, a typical number of the basis functions per atom for practical accuracy is roughly 10–20, which is comparable to the atomic-like basis case [3]. However the latter case has drawbacks such as the lack of systematic convergence.

There is a similar approach that utilizes the KS orbitals of subsystems as a basis set

for evaluating the Green's functions, though the method is specialized for a quasi-1D system [22]. In contrast, our scheme is the post-processing method of DC-DFT for a direct diagonalization of the Hamiltonian matrix. DC-DFT can be systematically applied to general 3D systems.

3.2   Basis set

The basis functions of the present method are constructed as follows. We introduce a cutoff energy ε_{cut} for the energy eigenvalues of the fragment orbitals in order to restrict the number of the fragment orbitals used for constructing the basis set:

$$\phi_i^\alpha(\mathbf{r}), \ (i = 1, \cdots, N_\alpha), \tag{3.1}$$

where N_α is the number of the fragment orbitals satisfying $\varepsilon_i^\alpha < \varepsilon_{cut}$, and i is the orbital index.

In order to eliminate a redundant contribution from the buffer region, we project the fragment wave functions onto Ω_0^α,

$$|\phi_i^\alpha\rangle \longrightarrow |\bar{\phi}_i^\alpha\rangle = \int_{\mathbf{r}\in\Omega_0^\alpha} d^3r |\mathbf{r}\rangle\langle\mathbf{r}|\phi_i^\alpha\rangle. \tag{3.2}$$

To avoid overcompleteness with the projected orbitals, we construct a smaller set of orbitals from them. Namely, we define an overlap matrix within each fragment α,

$$S_{ij}^\alpha = \langle\bar{\phi}_i^\alpha|\bar{\phi}_j^\alpha\rangle, \quad (i, j = 1, \cdots, N_\alpha). \tag{3.3}$$

Next, we diagonalize it,

$$S^\alpha \longrightarrow (U^\alpha)^\dagger S^\alpha U^\alpha = \text{diag}(\lambda_1^\alpha, \lambda_2^\alpha, \cdots, \lambda_{M_\alpha}^\alpha, 0, 0, \cdots), \tag{3.4}$$

where U^α and λ_i^α are the transformation matrix and the eigenvalue of S^α, respectively, and $M_\alpha \equiv \text{rank}\, S^\alpha$ is the number of the linearly independent eigenvectors. Practically, we set a sufficiently small cutoff parameter λ_{cut} for the eigenvalues $\lambda_i^\alpha (> \lambda_{cut})$ in order to control M_α .

The new basis functions are defined as,

$$|\lambda_i^\alpha\rangle = \frac{1}{\sqrt{\lambda_i^\alpha}} \sum_{j=1}^{N_\alpha} |\bar{\phi}_j^\alpha\rangle U_{ji}^\alpha, \quad (i = 1, \cdots, M_\alpha). \tag{3.5}$$

It is notable that these basis functions are orthonormal:

$$\langle\lambda_i^\alpha|\lambda_j^\beta\rangle = \delta_{\alpha,\beta}\delta_{i,j}. \tag{3.6}$$

23
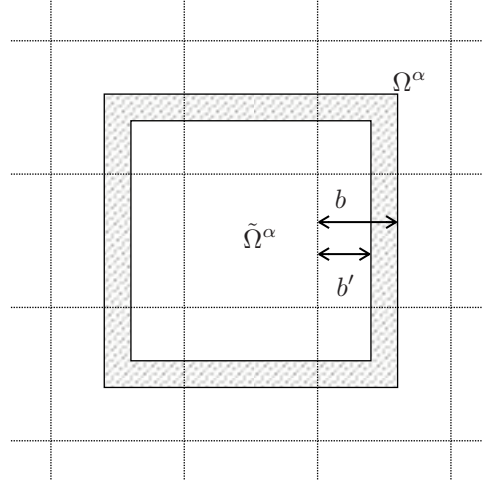
Figure 3.1: 2D schematic of the Hamiltonian matrix construction. To truncate the Hamiltonian, we introduce the projection operator $\hat{P}^\alpha$ corresponding to $\tilde{\Omega}^\alpha$. The buffer thickness b' of $\tilde{\Omega}^\alpha$ is restricted in $0 \le b' \le b$.

(a)   (b)
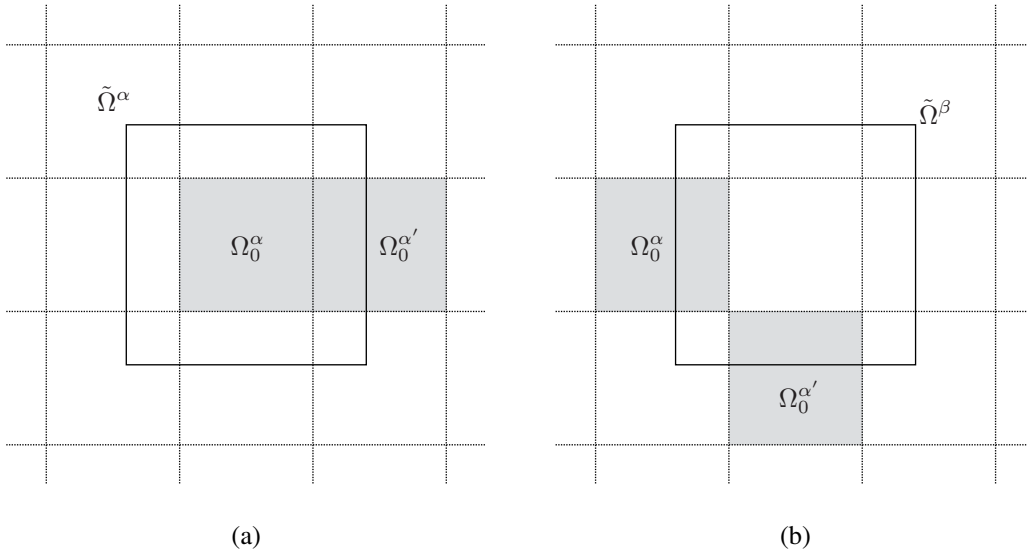
Figure 3.2: 2D schematic of the Hamiltonian matrix construction. (a) The projection operator $\hat{P}^\alpha$ is inserted in $\langle \lambda_{i'}^{\alpha'} | \hat{H} | \lambda_i^\alpha \rangle$, where α and α' are the first-nearest-neighbor fragments. (b) The projection operator $\hat{P}^\beta$ is inserted in $\langle \lambda_{i'}^{\alpha'} | \hat{H} | \lambda_i^\alpha \rangle$, where α and α' are the second-nearest-neighbor fragments in the 2D system, and β is the fragment overlapping with both α and α'.

24

3.3 Hamiltonian matrix

We shall construct the Hamiltonian matrix $H_{\alpha'i',\alpha i} \equiv \langle \lambda_{i'}^{\alpha'} | \hat{H} | \lambda_i^{\alpha} \rangle$, where $\hat{H} = -\frac{1}{2}\nabla^2 + \hat{V}_{\mathrm{KS}}$ is the conventional KS Hamiltonian operator of the total system. A straightforward approach to this calculation is real-space integeration, for example, $\langle \lambda_{i'}^{\alpha'} | \hat{V}_{\mathrm{KS}}^{\mathrm{local}} | \lambda_i^{\alpha} \rangle = \int d^3r \langle \lambda_{i'}^{\alpha'} | \mathbf{r} \rangle V_{\mathrm{KS}}^{\mathrm{local}}(\mathbf{r}) \langle \mathbf{r} | \lambda_i^{\alpha} \rangle$, etc. In the below, however, we show the Hamiltonian matrix elements can be evaluated from the fragment orbital energies without the numerically demanding integration.

The local part of the Hamiltonian has only diagonal blocks ($\alpha' = \alpha$) because of the non-overlapping nature of $|\lambda_i^{\alpha}\rangle$. On the other hand, the nonzero off-diagonal blocks ($\alpha' \neq \alpha$) come from the kinetic term $-\frac{1}{2}\nabla^2$ and the non-local potential term. In the DC scheme, it is assumed that the non-local terms decay within the buffer region Γ^{α}. It means that the terms decay within neighbor core domains, because the thickness of Γ^{α} is assumed as the same or the half length of each core domain Ω_0^{α} (Sec. 2.2.2). Following this assumption, we consider only the diagonal blocks ($\alpha' = \alpha$) and the off-diagonal blocks ($\alpha' \neq \alpha$) between the face-, edge- and corner-sharing neighboring core domains.

We shall obtain an approximate expression for the Hamiltonian matrix, which is represented by the KS orbitals and eigenenergies of a certain fragment overlapping with the core domains Ω_0^{α} and $\Omega_0^{\alpha'}$. The apparent absence of the Hamiltonian operator in the resulting expression allows us a consistent treatment regardless of whether or not whether numerically demanding non-local operators (e.g., exact exchange operator) are considered in the calculation within each fragment. The pivotal approximation is that the basis function $|\lambda_i^{\alpha}\rangle$ does not spill far out of the core domain through the Hamiltonian operation.

Now we define a projection operator for the Hamiltonian decomposition,

$$\hat{P}^{\alpha} = \int_{\mathbf{r} \in \tilde{\Omega}^{\alpha}} d^3r |\mathbf{r}\rangle\langle\mathbf{r}|, \tag{3.7}$$

where $\tilde{\Omega}^{\alpha}$ is a region to truncate the spillage of the basis functions upon the Hamiltonian operation (Fig. 3.3). Using the projection operator, we get the following exact expression,

$$\begin{aligned}
\hat{H}|\lambda_i^{\alpha}\rangle &= \hat{P}^{\alpha}\hat{H}|\lambda_i^{\alpha}\rangle + \hat{Q}^{\alpha}\hat{H}|\lambda_i^{\alpha}\rangle \\
&= \hat{P}^{\alpha}\hat{H}\hat{P}^{\alpha}|\lambda_i^{\alpha}\rangle + \hat{Q}^{\alpha}\hat{H}|\lambda_i^{\alpha}\rangle,
\end{aligned} \tag{3.8}$$

where $\hat{Q}^{\alpha} = \hat{1} - \hat{P}^{\alpha}$. Furthermore, the projected total Hamiltonian $\hat{P}^{\alpha}\hat{H}\hat{P}^{\alpha}$ can be converted to the fragment Hamiltonian $\hat{P}^{\alpha}\hat{H}^{\alpha}\hat{P}^{\alpha}$ due to a feature of $v_{\mathrm{bc}}^{\alpha}(\mathbf{r})$ that vanishes at the core domain Ω_0^{α}. The second term is presumably small if the range of $\tilde{\Omega}^{\alpha}$ is sufficiently larger than Ω_0^{α}. Therefore the Hamiltonian $\hat{H}$ acting on the vector $|\lambda_i^{\alpha}\rangle$ can be reasonably approximated as $\hat{P}^{\alpha}\hat{H}^{\alpha}\hat{P}^{\alpha}$.

Thus we get to the following approximate form of the Hamiltonian matrix element,

$$H_{\alpha'i',\alpha i} \approx \langle \lambda_{i'}^{\alpha'} | \hat{P}^{\alpha}\hat{H}^{\alpha}\hat{P}^{\alpha} | \lambda_i^{\alpha} \rangle. \tag{3.9}$$

From the range of the projector $\hat{P}^{\alpha}$, it is obviously nonzero only for α' whose core domain $\Omega_0^{\alpha'}$ is overlapping with $\tilde{\Omega}^{\alpha}$ (Fig. 3.2a). Since the fragment Hamiltonian $\hat{H}^{\alpha}$ can be

represented through the fragment orbitals $\{\phi_i^\alpha\}_{i=1}^\infty$, we obtain,

$$
\begin{aligned}
\langle \lambda_{i'}^{\alpha'} | \hat{P}^\alpha \hat{H}^\alpha \hat{P}^\alpha | \lambda_i^\alpha \rangle
&= \langle \lambda_{i'}^{\alpha'} | \hat{P}^\alpha \left(\sum_{j=1}^\infty \varepsilon_j^\alpha |\phi_j^\alpha\rangle\langle\phi_j^\alpha| \right) \hat{P}^\alpha | \lambda_i^\alpha \rangle \\
&= \sum_{j=1}^\infty \varepsilon_j^\alpha \langle \lambda_{i'}^{\alpha'} | \tilde{\phi}_j^\alpha \rangle \langle \tilde{\phi}_j^\alpha | \lambda_i^\alpha \rangle \\
&\approx \sum_{j=1}^{N_\alpha} \varepsilon_j^\alpha \langle \lambda_{i'}^{\alpha'} | \tilde{\phi}_j^\alpha \rangle \langle \tilde{\phi}_j^\alpha | \lambda_i^\alpha \rangle,
\end{aligned}
\tag{3.10}
$$

where $\tilde{\phi}_j^\alpha \equiv \hat{P}^\alpha \phi_j^\alpha$. Here, we reduced the high-energy region ($> \varepsilon_{\mathrm{cut}}$) for approximation.

While we introduced $\hat{P}^\alpha \hat{H}^\alpha \hat{P}^\alpha$ as explained above, we mention here that Eq. (3.9) can be generalized as follows:

$$
H_{\alpha' i', \alpha i} \approx \langle \lambda_{i'}^{\alpha'} | \hat{P}^\beta \hat{H}^\beta \hat{P}^\beta | \lambda_i^\alpha \rangle,
\tag{3.11}
$$

where β is an arbitrary fragment satisfying $\tilde{\Omega}^{\alpha'} \cap \tilde{\Omega}^\alpha \subset \tilde{\Omega}^\beta$ (for example, see Fig. 3.2b). We have found that the choice of $\hat{P}^\beta \hat{H}^\beta \hat{P}^\beta$ has quantitatively no effect on results.

Combining Eq. (3.9) and Eq. (3.10), we can represent the matrix elements of the total Hamiltonian with the fragment orbitals $\{\phi_i^\alpha\}$ and the eigenenergies $\{\varepsilon_i^\alpha\}$, namely the output of DC-DFT. Note that the controllable parameters in our eigenstate calculation method are $\varepsilon_{\mathrm{cut}}$, λ_{cut}, and the buffer thickness b' of $\tilde{\Omega}^\alpha$ ($0 \le b' \le b$, see Fig. 3.3).

We need some consideration for the optimum thicknesses b' and b. The thickness b is dictated by the nearsightedness principle [46, 47] in the conventional DC algorithms (Sec. 2.2.1). On the other hand, the thickness b' is determined by the decay range of the non-local term of the KS Hamiltonian. Although large value of b and b' may improve results of the calculation, there is a possibility that the $b' \to b$ limit degrade the accuracy because of the artificial boundary conditions at $\partial\Omega^\alpha$. Thus it seems that accuracy requirements for our method demand a large b value which can fully contain the nearsightedness range (conventional b) plus the Hamiltonian decay range (b'). However, following results show this is not the case. In fact, for the LDC-DFT-based scheme, the $b' = b$ limit leads to the best results in eigenstate calculations (see Sec. 4.1.2). This might be attributed to the fact that the uniform kinetic-energy term is the main factor of the non-local part. Moreover, we can deduce that the periodic boundary conditions at the fragment boundaries $\partial\Omega^\alpha$ also improve the accuracy of the eigenstates in condensed matter. If we utilized other boundary conditions (e.g. insertion of artificial vacuum regions [28, 29]), the accuracy for the eigenstates might require an optimization of the b' value.

In the above argument, the Hamiltonian matrix has the periodicity of the whole supercell. Namely, the electronic state derived from DC-LCFO corresponds to that of the Γ-point calculation in the total system. Also we can evaluate the electronic state with the k-point sampling by using modified DC-LCFO Hamiltonian (see Appendix. B). Hence we can calculate, for example, energy bands without the recalculation of the electron density.

3.4 Exact exchange potential

The exact exchange, or Hartree-Fock, potential Eq. (2.9) can be also contained in the total Hamiltonian as a non-local term. This operator can be rewrite as,

$$
\begin{aligned}
[\hat{V}_{\mathrm{x}}^{\mathrm{HF}}\psi_i](\mathbf{r}) &= -\sum_j^{\mathrm{occ}} \psi_j(\mathbf{r}) \int d^3 r' \frac{\psi_j^*(\mathbf{r}')\psi_i(\mathbf{r}')}{|\mathbf{r}-\mathbf{r}'|} \\
&= -\int d^3 r' \frac{\rho(\mathbf{r},\mathbf{r}')\psi_i(\mathbf{r}')}{|\mathbf{r}-\mathbf{r}'|},
\end{aligned}
\tag{3.12}
$$

where $\{\psi_i(\mathbf{r})\}$ are orbital wavefunctions of the total system and $\rho(\mathbf{r},\mathbf{r}')$ is the density matrix Eq. (1.5). As mentioned in Sec. 1.2, the density matrix is localized with respect to $|\mathbf{r}-\mathbf{r}'|$ in many cases. Therefore we can take into account only the short-range part of $\hat{V}_{\mathrm{x}}^{\mathrm{HF}}$ and adopt the DC scheme in such cases. It is expected that our method allows high-speed eigenstate calculations within hybrid functionals. In a naive implementation of the exact exchange, the computational cost is proportional to the fourth power of the system size. On the other hand, in the present method, the computational cost of the Hamiltonian construction is negligible and the cost of the diagonalization is proportional to the third power of the small matrix dimension as explained in Sec. 3.1.

In Sec. 4.2, we perform the simple DC-LCFO calculations with the hybrid functional to demonstrate the performance of our method. Namely, after doing the conventional calculation including the exact exchange in each fragment independently, we construct the basis set $\{|\lambda_i^{\alpha}\rangle\}$ and the Hamiltonian matrix $\{H_{\alpha'i',\alpha i}\}$ from the orbitals derived by these calculations. The result of this calculation shows that use of hybrid functionals makes no difference to the computational time for DC-LCFO. In Sec. 5.1 and Sec. 5.2, we see that the DC-LCFO calculation with the exact exchange yields reasonable accuracy for the defect state.

3.5 Unphysical zero eigenvalues

3.5.1 Avoidance of unphysical zero eigenvalues

In Sec. 3.2, we presented the method for removing overcompleteness in the basis set. However, we have found that the Hamiltonian matrix defined by the basis functions Eq. (3.5) has enormous zero eigenvalues. This indicates that the Hamiltonian matrix contains unphysical eigenvectors in spite of absence of overcompleteness in the basis set. We need a technique to avoid the zero eigenvalues in the resultant eigenenergies or to remove the unphysical eigenvectors. The latter technique will be discussed in the next subsection, and we shall argue the former technique in this subsection.

To avoid the zero eigenvalues, we shift the energy origin as $\varepsilon_i^{\alpha} \longrightarrow \varepsilon_i^{\alpha} - \varepsilon_{\mathrm{cut}}$. Namely, Eq. (3.10) is changed as

$$
H_{\alpha'i',\alpha i} \approx \sum_{j=1}^{N_\alpha} (\varepsilon_j^{\alpha} - \varepsilon_{\mathrm{cut}})\langle\lambda_{i'}^{\alpha'}|\tilde{\phi}_j^{\alpha}\rangle\langle\tilde{\phi}_j^{\alpha}|\lambda_i^{\alpha}\rangle.
\tag{3.13}
$$

The negative eigenvalues $\{\varepsilon_i\}$ of the matrix $\{H_{\alpha'i',\alpha i}\}$ coincide with the physical eigenenergies of the total system. Needless to say, the true eigenenergies can be obtained by the pullback: $\varepsilon_i \longrightarrow \varepsilon_i + \varepsilon_{\text{cut}}$. The unphysical zero eigenvalues are then accumulated at the vicinity of ε_{cut}. With this technique, the unphysical vectors does not affect the accuracy on the low-energy electronic properties (see Fig.4.7 and Fig. 4.8).

3.5.2 Further reduction of the basis set size

In Sec. 3.2, we formulated the basis set from the fragment orbitals,

$$\{\, |\phi_i\rangle \mid \varepsilon_i < \varepsilon_{\text{cut}} \} \longrightarrow \{\, |\lambda_i\rangle \, \}. \tag{3.14}$$

As mentioned in the preceding section, the Hamiltonian matrix contains many unphysical eigenvectors and has a large dimension. Let us argue a procedure for further reduction of the basis set size. In this section, we discuss within a specific fragment and omit the fragment index α of the fragment orbitals and their orbital energies for brevity.

We define a fragment Hamiltonian matrix H' (do not confuse this with the total Hamiltonian of the whole system) as follows:

$$
\begin{aligned}
H'_{ij} &= \sum_{k=1}^{N_\alpha} \langle \lambda_i | \phi_k \rangle (\varepsilon_k - \varepsilon_{\text{cut}}) \langle \phi_k | \lambda_j \rangle \\
&= \sum_{k=1}^{N_\alpha} \langle \lambda_i | \bar{\phi}_k \rangle (\varepsilon_k - \varepsilon_{\text{cut}}) \langle \bar{\phi}_k | \lambda_j \rangle \\
&= \frac{1}{\sqrt{\lambda_i \lambda_j}} \sum_{k=1}^{N_\alpha} (\varepsilon_k - \varepsilon_{\text{cut}}) [U^\dagger S]_{ik} [S U]_{kj} \\
&= \frac{1}{\sqrt{\lambda_i \lambda_j}} \sum_{k=1}^{N_\alpha} (\varepsilon_k - \varepsilon_{\text{cut}}) [S U]_{ki}^* [S U]_{kj},
\end{aligned}
\tag{3.15}
$$

where $i, j = 1, \cdots, M_\alpha$ and we used Eq. (3.5). S and U are $N_\alpha \times N_\alpha$ matrices defined in Eq. (3.3) and Eq. (3.4), respectively. The matrix H' is identical to the block matrix separated from the total Hamiltonian. The matrix is diagonalized as

$$U'^\dagger H' U' = \text{diag}(\varepsilon'_1, \cdots, \varepsilon'_{M_\alpha}). \tag{3.16}$$

We set a new controllable parameter $\varepsilon'_{\text{cut}}$ ($\leq \varepsilon_{\text{cut}}$) and take the eigenvectors of H' whose eigenvalue is smaller than $\varepsilon'_{\text{cut}}$. A new basis vectors are defined as,

$$|\lambda'_i\rangle = \sum_{j=1}^{M_\alpha} |\lambda_j\rangle U'_{ji}, \quad (i = 1, \cdots, M'_\alpha), \tag{3.17}$$

where M'_α is the number of the eigenvalues ε'_i satisfying

$$\varepsilon'_i + \varepsilon_{\text{cut}} < \varepsilon'_{\text{cut}}. \tag{3.18}$$

When $\varepsilon'_{\text{cut}} = \varepsilon_{\text{cut}}$, Eq. (3.17) is the unitary transformation, so that this procedure yields no change for the results.

The above procedure is analogous to the reduction procedure in Sec. 3.2, with a replacement $|\bar{\phi}_i\rangle \longrightarrow |\lambda_i\rangle$, $S \longrightarrow -H'$, $U \longrightarrow U'$ and $\lambda_{\text{cut}} \longrightarrow \varepsilon_{\text{cut}} - \varepsilon'_{\text{cut}}$. With this analogy, the unphysical eigenvectors of the total Hamiltonian matrix is understood as the overcompleteness of the "overlap matrix" $-H'$. Furthermore, we can deduce that a large value of $\varepsilon_{\text{cut}} - \varepsilon'_{\text{cut}}$ may degrade the accuracy of the resultant eigenstates. In other words, there is a tradeoff between the accuracy and the basis set size in a similar way to λ_{cut}.

3.6 Implementations

3.6.1 Implementation of the LDC-DFT code

We have implemented LDC-DFT [31] in the xTAPP code [49]. The program is parallelized using the message passing interface (MPI) library with two levels of parallelism. In the first level, each fragment is assigned a number of MPI processes and these process groups are separated each other by MPI_COMM_SPLIT subroutine. In the second level, the electronic state calculations for each fragment are parallelized with MPI processes which have their respective reciprocal-space grid points in the fragment.

The fragment orbitals are diagonalized by the standard plane-wave calculation and the fast Fourier transformations (FFT) within each fragment. The orbitals correspond to the Bloch states at Γ-point in unit cell Ω^α. The calculation of the global chemical potential μ requires the real-space integration of the fragment orbitals within the core domain. The electron densities for the fragments are combined with MPI_ALLREDUCE subroutine. To calculate the local potential, the global FFT process for the total density is required. The Hartree potential is obtained globally by solving the Poisson equation in the reciprocal space. The update of the potential is performed by the Anderson potential mixing method [50].

3.6.2 Implementation of the DC-LCFO code

We have also implemented DC-LCFO in the preceding code. The fragment orbitals are transformed into the real functions in the real space by FFT. To perform our method, we use the grid points of FFT for the projection and the inner-product operations for the fragment orbitals (Sec. 3.2).

The overlap matrix and the Hamiltonian matrix are defined as real-symmetric matrices. The operations to generate the basis functions and the diagonal blocks of the total Hamiltonian matrix are completely parallelized, while the calculation for the off-diagonal blocks requires MPI point-to-point communications using MPI_SEND and MPI_IRECV subroutines. The matrix elements of the total Hamiltonian are assembled in the root process with MPI_GATHER subroutine. Finally the total Hamiltonian matrix is diagonalized by a serial computation. All the diagonalizations of the matrices are done with DSYEV subroutine of LAPACK library.

The orbital wavefunctions of the whole system are obtained from the basis functions and the unitary matrix of the diagonalization for the total Hamiltonian. For this calculation, the basis functions in the respective fragments are gathered in the root process with MPI_GATHER subroutine.

3.6.3 Computational details

In the following calculations, we used the plane-wave basis (for calculations in each fragment), the norm-conserving pseudopotentials, and PBE exchange-correlation functional [43] except some calculations with the exact exchange, in which PBE0 hybrid functional [44] was used. For the PBE0 calculation, we used a cutoff parameter R_c [51,52] for truncating the Coulomb potential $1/|\mathbf{r} - \mathbf{r}'|$ in the exact exchange Eq. (2.9):

$$
v(\mathbf{r}) = \begin{cases} 1/|\mathbf{r}| & (|\mathbf{r}| \le R_c) \\ 0 & (|\mathbf{r}| > R_c) \end{cases}.
\tag{3.19}
$$

Needless to say, R_c should be set as $R_c < b'$ for DC-LCFO.

All the calculations were carried out in the paramagnetic case. For comparison we also performed the conventional DFT calculations, where we sampled the Brillouin zone at the Γ point ($\mathbf{k} = 0$ point).

Chapter 4

Analysis of parameter dependence and Benchmark tests

4.1 Parameter dependence

4.1.1 Introduction

We shall analyze a parameter dependence for the eigenenergies calculated with our method on b', λ_{cut} and ε_{cut}. We also examine the $\varepsilon'_{\text{cut}}$ dependence for the reduction scheme described in Sec. 3.5.2. The parameter dependence analyzed in this section gives a guide for proper selection of the parameters in applications.

We use two systems: SiC 512-atom $4 \times 4 \times 4$ supercells with the zinc-blende structure and "amorphous" structures (Fig. 4.1). The latter structure was obtained by a high-temperature MD simulation (with the microcanonical ensemble, T=8000 K). In this MD simulation, we omitted the cooling process since our purpose is simply to examine the eigenstate of a disordered system. We divide the systems into 64 fragments with $4 \times 4 \times 4$ configurations, respectively. The edge lengths of each cubic core domain and the buffer thickness b are fixed as a = 4.39 Å (experimental lattice constant) so that the fragment is $3 \times 3 \times 3$ cell. The plane-wave cutoff is 30 Ry and the number of the FFT mesh points is equal to $16 \times 16 \times 16$ in each core domain.

We shall show and discuss the root mean square (RMS) errors of the occupied eigenenergies with respect to the results of the conventional caluculations. Here, RMS error of n eigenenergies is defined as follows:

$$\text{RMS error} = \sqrt{\frac{1}{n} \sum_{i}^{n} (\varepsilon_i - \varepsilon_i^0)^2}, \tag{4.1}$$

where ε_i and ε_i^0 are the eigenenergy for the total system obtained by our method and the conventional DFT calculation, respectively. In Sec. 4.1.2–4.1.4, we analyze the parameter dependence on b', λ_{cut} and ε_{cut} without the reduction scheme. In Sec. 4.1.5, we show an effectiveness of the reduction scheme.
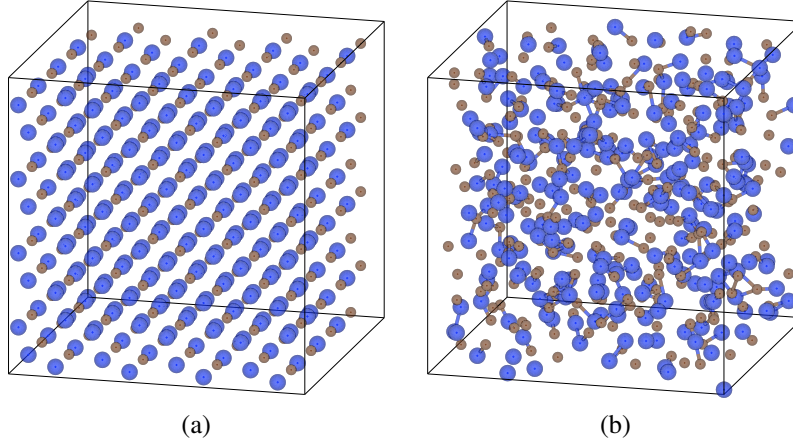
Figure 4.1: Atomic configurations of 512-atom SiC supercells with (a) the zinc-blende and (b) amorphous structures, depicted with VESTA [53].

4.1.2 b' dependence

Figure 4.2 shows the relation between the thicknesses b' and RMS errors, where the other parameters are fixed as $\varepsilon_{\text{cut}} - \mu = 10.88$ eV (0.4 Hartree) and $\lambda_{\text{cut}} = 10^{-3}$.

This figure suggests that $b' = b$ leads to the best results. The behavior of the error in the zinc-blende structure can be easily accepted as the periodic structure of the fragments. On the other hand, the behavior for the disordered structure indicates that effects of the artificial boundary may not be harmful for the accuracy of the eigenstate (see the last paragraph of Sec. 3.3). With these results, we set $b' = b$ in all the following calculations.

We also point out the relation between b' and the Laplacian of the finite difference method. The leading term in non-local parts of the Hamiltonian is the kinetic term, or the Laplacian term. In the finite differences method, recalling Eq. (1.3), the range of the Laplacian is given by the grid spacing h and the order of expansion M. Our $b' = b$ value in this section sufficiently exceeds the Laplacian range for the practical finite-differences calculations (see Fig. 2 in Ref. [32]).

4.1.3 λ_{cut} dependence

Let us change λ_{cut} value from 10^{-1} to 10^{-5} and analyze the relation between the errors and the matrix size. Figure 4.3 is the RMS errors plotted against the number of the basis functions ($\sum_{\alpha} M_{\alpha}$) per atom with the parameter $\varepsilon_{\text{cut}} - \mu = 10.88$ eV (0.4 Hartree). The figure suggests the speed-accuracy tradeoff relation and indicates that the RMS errors are saturated at nearly 16 basis functions per atom when $\lambda_{\text{cut}} = 10^{-3}$.

4.1.4 ε_{cut} dependence

Figure 4.4 illustrates the ε_{cut} dependence of the RMS errors with the same conditions, where the energy origin is fixed at the chemical potential μ (= the conduction band mini-
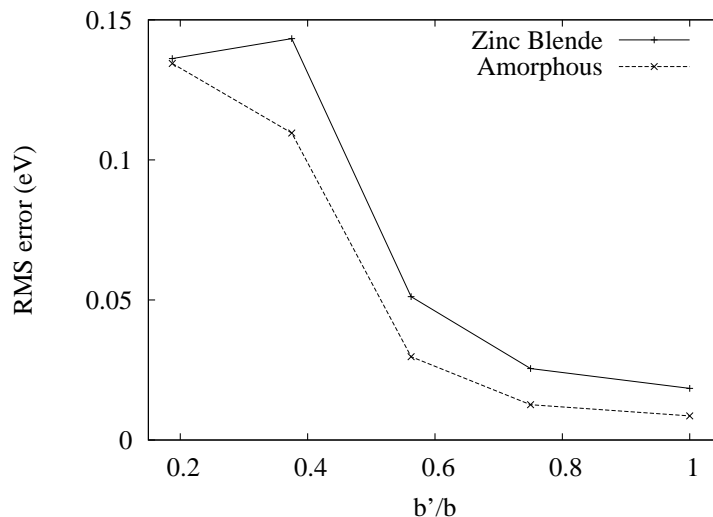
Figure 4.2: RMS error of the occupied eigenenergies as a function of a ratio b'/b for SiC systems with zinc-blende structure and amorphous structure, where each system contains 512 atoms in a cubic $4 \times 4 \times 4$ supercell. The other parameters are fixed as $\varepsilon_{\text{cut}} - \mu = 10.88$ eV (0.4 Hartree) and $\lambda_{\text{cut}} = 10^{-3}$.
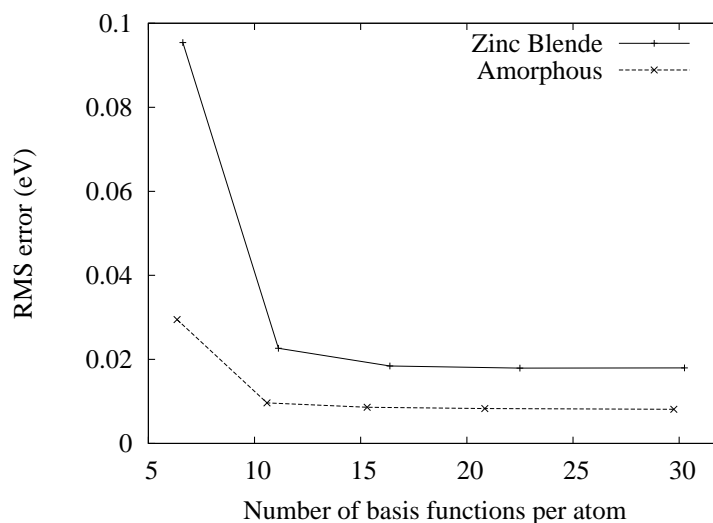
Figure 4.3: RMS errors plotted against a number of the basis functions per atom for the same systems as Fig. 4.2, where $b' = b$ and $\varepsilon_{\text{cut}} - \mu = 10.88$ eV (0.4 Hartree). These points correspond to $\lambda_{\text{cut}} = 10^{-1}$, 10^{-2}, 10^{-3}, 10^{-4}, and 10^{-5} respectively from left to right.
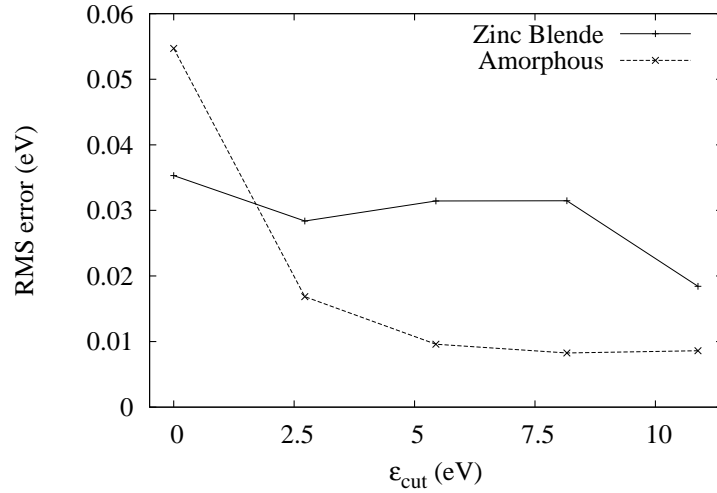
Figure 4.4: ε_{cut} dependence of the RMS errors for the same systems as Fig. 4.2, where the energy origin is fixed at the Fermi energy μ. The other parameters are fixed as $b' = b$ and $\lambda_{cut} = 10^{-3}$.
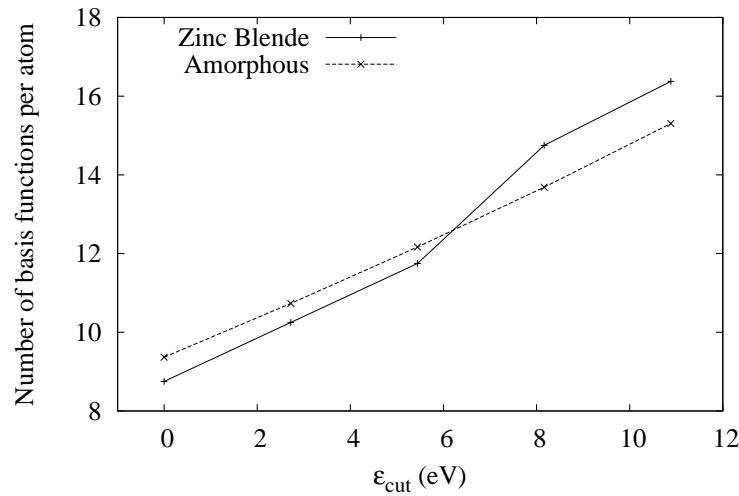
Figure 4.5: Relation between ε_{cut} and the number of the basis functions per atom for the same systems as Fig. 4.2. Here, $b' = b$ and $\lambda_{cut} = 10^{-3}$. The energy origin is fixed at the chemical potential μ.
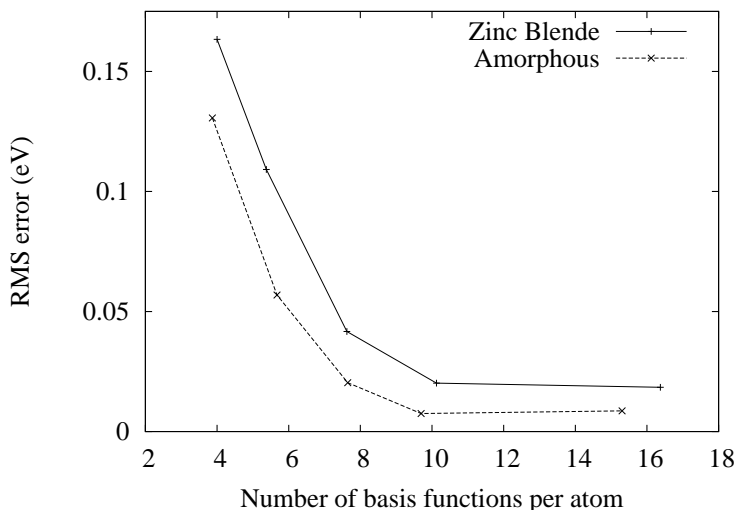
Figure 4.6: RMS errors against to the number of the basis functions per atom by changing $\varepsilon'_{\text{cut}}$ for the same systems as Fig. 4.2. These points correspond to $\varepsilon_{\text{cut}} - \varepsilon'_{\text{cut}} = 10^{-1}, 10^{-1.5}$, $10^{-2}, 10^{-2.5}$ and 0 (in Hartree) respectively from left to right. Here, $b' = b$, $\lambda_{\text{cut}} = 10^{-3}$ and $\varepsilon_{\text{cut}} - \mu = 10.88$ eV (0.4 Hartree).

mum in a gapped system).

In the amorphous structure, the eigenenergies of the occupied states are accurately evaluated with a large ε_{cut} value. On the other hand, the error for the zinc-blende structure indicates weak dependence on ε_{cut} probably due to the band gap. In a gapped state, we can deduce that it is sufficient to utilize the occupied fragment orbitals for representing the occupied states of the total system.

We also show the relation between ε_{cut} and the number of the basis functions per atom (Fig. 4.5), where $\lambda_{\text{cut}} = 10^{-3}$. The basis size grows proportional to ε_{cut} as might have been supposed.

4.1.5 Further reduction: $\varepsilon'_{\text{cut}}$ dependence

Finally we examine the effectiveness of the reduction scheme of Sec. 3.5.2. The parameters are fixed as $\varepsilon_{\text{cut}} - \mu = 10.88$ eV (0.4 Hartree) and $\lambda_{\text{cut}} = 10^{-3}$. Figure 4.6 shows the basis size dependence of the RMS errors by changing the $\varepsilon'_{\text{cut}}$ value. The points in Fig. 4.6 correspond to $\varepsilon_{\text{cut}} - \varepsilon'_{\text{cut}} = 10^{-1}, 10^{-1.5}, 10^{-2}, 10^{-2.5}$ and 0 (in Hartree) respectively from left to right. In the $\varepsilon'_{\text{cut}} = \varepsilon_{\text{cut}}$ case, the reduction is not performed.

Figure 4.6 resembles the λ_{cut} dependence Fig. 4.3, which is expected in the last paragraph of Sec. 3.5.2. The reduction scheme decreases the basis size without compromise of the accuracy when $\varepsilon_{\text{cut}} - \varepsilon'_{\text{cut}} = 10^{-2.5}$ Hartree. In this case, the numbers of the basis functions are reduced to two-thirds of the case without the reduction scheme.

35

4.1.6 Summary

In summary, the practical accuracy for the eigenstate requires the parameter values for $b' = b$, $\lambda_{\text{cut}} \approx 10^{-3}$, and a sufficiently large ε_{cut} value compared to the desired energy range. These conditions provide the accuracy comparable with FMO-LCMO [40, 41]. Moreover, the reduction scheme of Sec. 3.5.2 can reduce the number of the basis functions to two-third of the original basis set without compromise of the accuracy when $\varepsilon_{\text{cut}} - \varepsilon'_{\text{cut}} = 10^{-2.5}$ Hartree.

Before closing this section, we point out that our method can also describe the unoccupied states. Figure 4.7 and 4.8 illustrate the density of states for the zinc-blende structure and the disordered structure, respectively. Here the energy origin is fixed at the chemical potential μ. The disordered structure is metallized by the rough MD simulation. In the $\varepsilon_{\text{cut}} = 10.88$ eV (0.4 Hartree) case, the unoccupied states agree well with the conventional results. With this ε_{cut} value, the 3 highest occupied and the 3 lowest unoccupied orbitals are illustrated in Fig. 4.9 (Fig. 4.11) and Fig. 4.10 (Fig. 4.12) for the zinc-blende (disordered) structure, respectively. Here, we also describe the overlap integral between the corresponding orbitals obtained with DC-LCFO and the conventional calculation.

In the zinc-blende structure case, however, the DC-LCFO wavefunctions ($\{\psi_i^{\text{LCFO}}\}$) seem to disagree with those of the conventional case ($\{\psi_i^{\text{conv.}}\}$). This discrepancy comes from the hybridization of the degenerate states. We can resolve the hybridization with a following unitary transformation:

$$|\psi_i^{\text{LCFO}}\rangle \rightarrow \sum_j |\psi_j^{\text{LCFO}}\rangle\langle\psi_j^{\text{LCFO}}|\psi_i^{\text{conv.}}\rangle, \tag{4.2}$$

where the summation is over the degenerate states. We confirm the transformed states agree with the conventional results (see (g)–(i) of Fig. 4.9 and Fig. 4.10). These results show that DC-LCFO can reproduce not only occupied states but also unoccupied states with reasonable accuracy.

We also comment on the unphysical zero eigenvalues. In the $\varepsilon_{\text{cut}} = 5.44$ eV case of Fig. 4.7 and 4.8, unphysical states appear in the vicinity of ε_{cut}. These states correspond to the unphysical zero eigenvalues mentioned in Sec. 3.5.
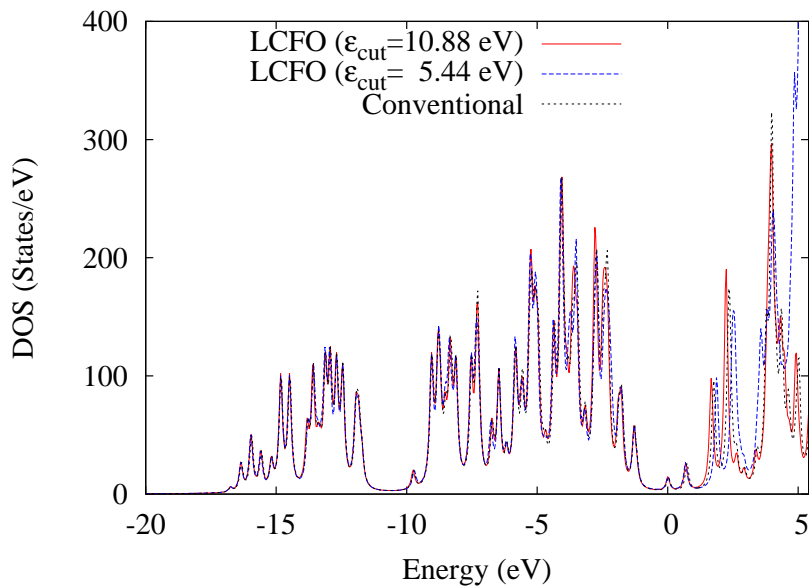
Figure 4.7: Density of states for the zinc-blende structure SiC. The energy origin is fixed at the chemical potential μ and the broadening of the Lorentzian function is 0.08 eV. DC-LCFO with ε_{cut} = 5.44 eV (blue-dashed line) indicates emergence of the unphysical eigenvalues in vicinity of ε_{cut}.
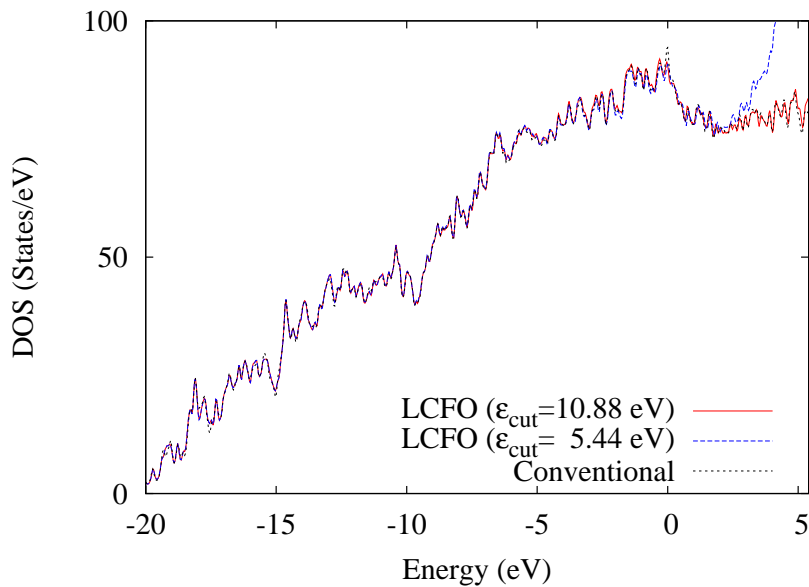
Figure 4.8: Same as Fig. 4.7, but for the amorphous structure. The system is metalized by the rough MD process (see the text).
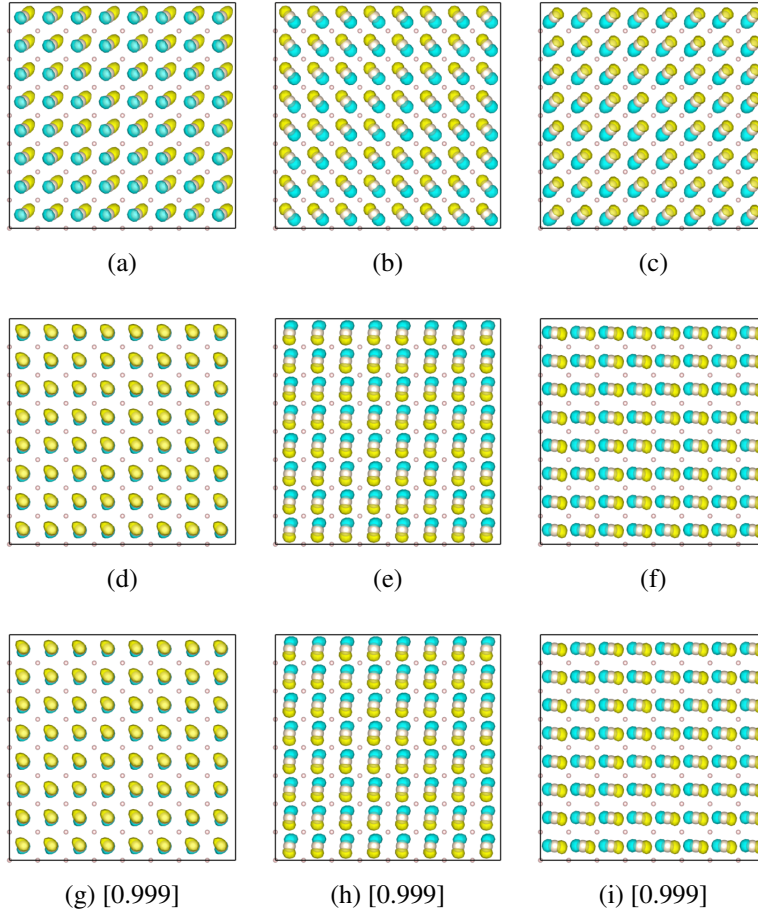
Figure 4.9: Wave functions of the 3 degenerate highest occupied states for the zinc-blende structure SiC. (a), (b) and (c) show DC-LCFO results without the unitary transformation. (d), (e) and (f) are the conventional results. (g), (h) and (i) are the unitary transformed wavefunctions of DC-LCFO, see Eq. (4.2). Here (g)–(i) are attached the value of the overlap with the corresponding conventional result (in square bracket).
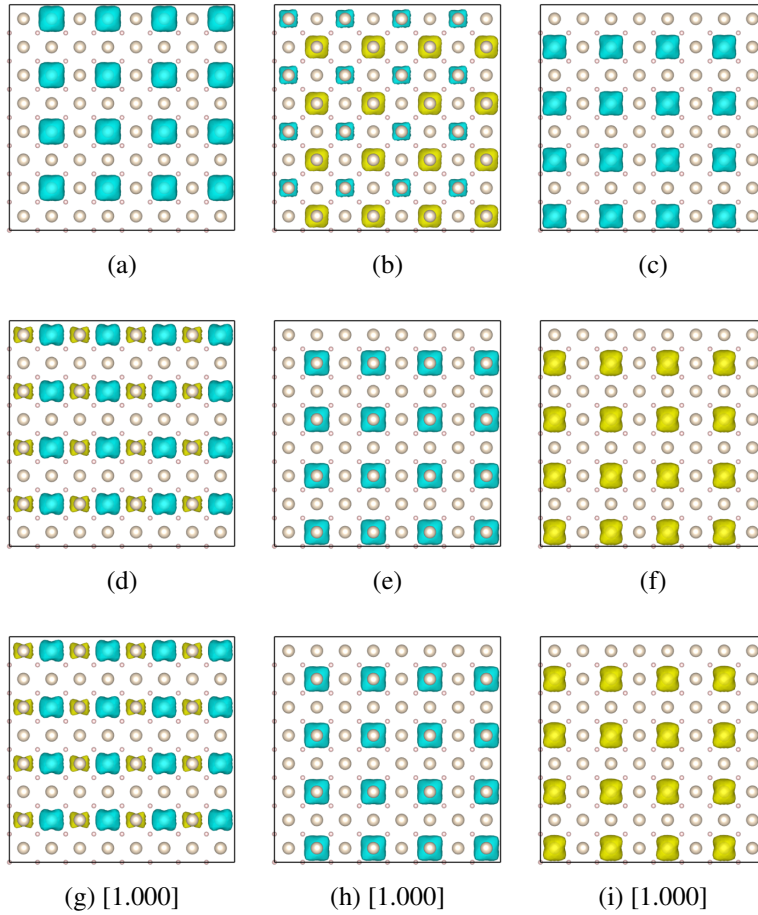
Figure 4.10: Wave functions of the 3 degenerate lowest unoccupied states for the zinc-blende structure SiC. (a), (b) and (c) show DC-LCFO results without the unitary transformation. (d), (e) and (f) are the conventional results. (g), (h) and (i) are the unitary transformed wavefunctions of DC-LCFO, with the value of the overlap with the corresponding conventional result (in square bracket).
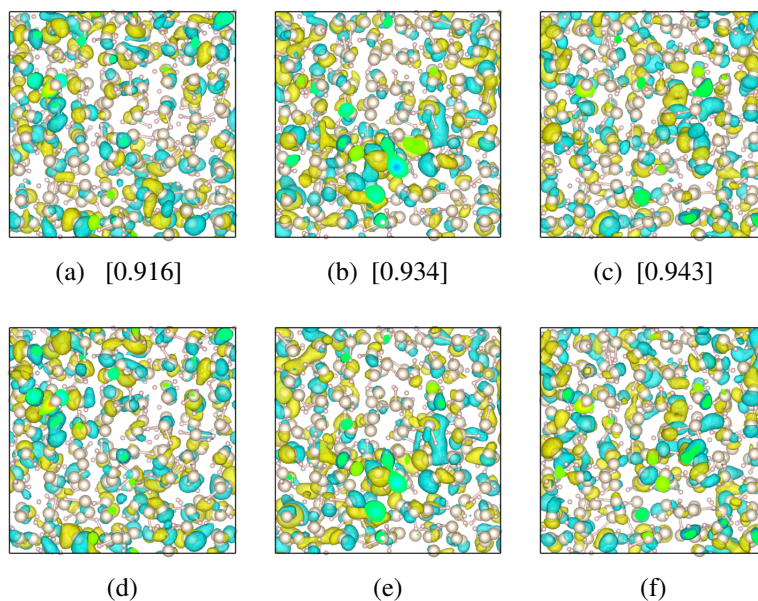
Figure 4.11: Wave functions of the 3 highest occupied states for the amouphous structure SiC. (a), (b) and (c) show DC-LCFO results. (d), (e) and (f) are the conventional results. The DC-LCFO results are attached the value of the overlap with the corresponding conventional result (in square bracket).

Figure 4.12: Wave functions of the 3 lowest unoccupied states for the amorphous structure SiC. (a), (b) and (c) show DC-LCFO results. (d), (e) and (f) are the conventional results. The DC-LCFO results are attached the value of the overlap with the corresponding conventional result (in square bracket).
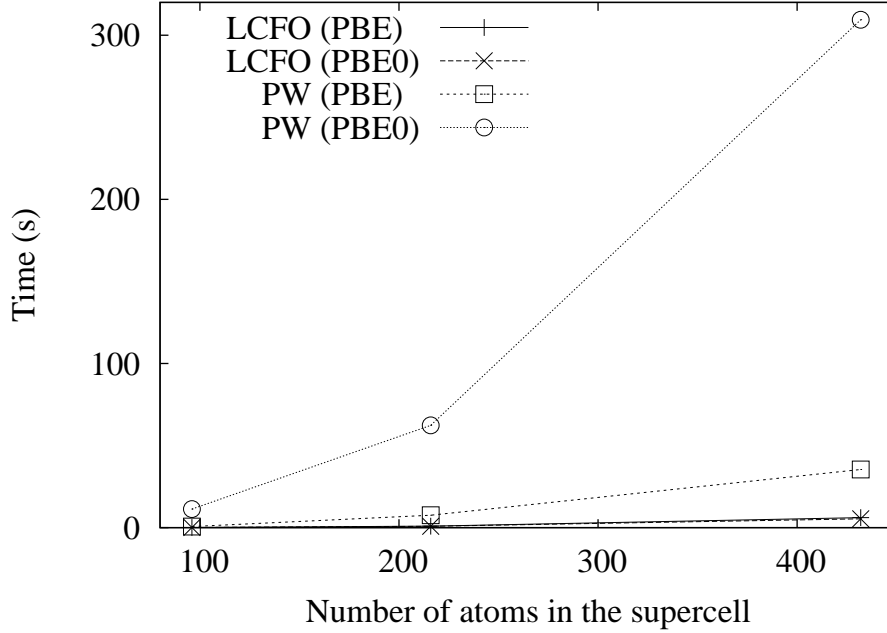
Figure 4.13: Computational cost of the Hamiltonian diagonalization (per iteration for the conventional cases) with different supercells, where the exchange-correlation functional is PBE or PBE0. LCFO indicates our method , while PW corresponds to the conventional plane-wave calculation. The computation is done on a 24-cores 2.5 GHz Intel Xeon cluster with 144 nodes.

4.2 Benchmark tests for the Hamiltonian diagonalization

We performed benchmark tests of the DC-LCFO method using Si 96-atom ($12 \times 1 \times 1$), 216-atom ($27 \times 1 \times 1$), and 432-atom ($54 \times 1 \times 1$) supercells to see the computational efficiency of DC-LCFO. The systems are divided into 12, 27, and 54 fragments along the x direction, respectively. We set $b = a$ (lattice constant) in the x direction and $b = 0$ in the y-z plane so that each fragment is equal to $3 \times 1 \times 1$ supercell. The basis set $\{|\lambda_i^\alpha\rangle\}$ and the Hamiltonian matrix $\{H_{\alpha'i',\alpha i}\}$ are derived from copied wave functions, which are obtained by the conventional calculation in the $3 \times 1 \times 1$ cell, where we used PBE and PBE0 functionals. We fixed the parameters as $b' = b$, $\lambda_{\text{cut}} = 10^{-3}$, and $N_\alpha = 56$ (= occupied + 8 orbitals, instead of ε_{cut}). For PBE0 calculation, we set the cutoff parameter of Eq. (3.19) as $R_{\text{c}} = 8$ a.u. $< b'$.

Figure 4.13 shows the computational time for the construction and diagonalization of the Hamiltonian (per iteration for the conventional cases), where the reduction scheme (Sec. 3.5.2) does not performed. This result indicates that our method enables a high-speed computation of the eigenstate, and the exact exchange potential makes no difference for the computational cost in DC-LCFO.

In Table 4.1, we show the details of the computational time for $54 \times 1 \times 1$ cell with also the reduction scheme case ($\varepsilon_{\mathrm{cut}} - \varepsilon'_{\mathrm{cut}} = 10^{-2.5}$ Hartree). The cost for the basis set construction becomes larger with the reduction scheme since it takes labor. However the diagonalization cost is reduced thanks to the small size of basis set (see Table 4.2). Note that the basis-set cost is $O(N)$ and not significant for large systems. In Table 4.2, we also describe the RMS error and the maximum absolute error (MAE) of the occupied eigenenergies, and the error of the band gap for $54 \times 1 \times 1$ cell.

Table 4.1: Details of the computational time (in seconds) for the Si $54 \times 1 \times 1$ cell. "full" and "reduced" indicate the case with and without the reduction scheme of Sec. 3.5.2. The exchange-correlation functional is PBE or PBE0. Total time consists of the time for constructing the basis set, the time for diagonalizing the Hamiltonian matrix, and residual time such as the inner-product operation or MPI communications. The parameters setup is given in the text.

	Basis set	Diagonalization	Total
PBE (full)	3.01×10^{-2}	6.04	6.13
PBE (reduced)	9.66×10^{-2}	1.74	1.94
PBE0 (full)	2.48×10^{-2}	5.25	5.35
PBE0 (reduced)	5.31×10^{-2}	3.43	3.54

Table 4.2: RMS error, MAE and error of the band gap (in eV) with respect to the conventional results for Table 4.1, where RMS error and MAE are calculated for occupied states. $N_{\mathrm{basis}}/N_{\mathrm{atom}}$ indicates the number of basis functions per atom.

	RMS (occ)	MAE (occ)	Error of Gap	$N_{\mathrm{basis}}/N_{\mathrm{atom}}$
PBE (full)	0.020	0.104	0.087	4.75
PBE (reduced)	0.022	0.112	0.082	3.38
PBE0 (full)	0.034	0.118	0.029	4.62
PBE0 (reduced)	0.035	0.124	-0.026	4.00

Chapter 5

Applications

5.1 Phosphorus doped Silicon

We shall demonstrate that our method can describe defect states with a spatially extended wave functions with satisfactory accuracy. To this end, we perform a calculation for a P-doped Si crystal that contains 512 atoms (one P atom included). The crystal structure of the $4 \times 4 \times 4$ supercell is determined as follows: Using the conventional xTAPP code, we optimized the structure of $3 \times 3 \times 3$ cell containing one P atom. Next, we attached the unoptimized Si unit cells around this $3 \times 3 \times 3$ cell.

We divide the system into 64 fragments with the $4 \times 4 \times 4$ configuration, where the side lengths of each core domain and the buffer thickness are fixed to $a = 5.43$ Å (experimental lattice constant). We perform the calculations with the GGA-PBE functional and the PBE0 hybrid functional. The cutoff parameter for the exact exchange potential R_c is set to 8 a.u. $= 4.23$ Å. The plane-wave cutoff is 30 Ry and the number of the FFT mesh points is equal to $18 \times 18 \times 18$ in each core domain.

The controllable parameters of the eigenstate calculation are set as $b' = b$, $\lambda_{cut} = 10^{-3}$, and $\varepsilon_{cut} - \mu = 8.163$ eV (0.3 Hartree) for the PBE calculation. We put $\varepsilon_{cut} - \mu = 1.361$ eV (0.05 Hartree) for the PBE0 calculation to economize the computational time. The parameter for the reduction scheme is set as $\varepsilon_{cut} - \varepsilon'_{cut} = 10^{-2.5}$ Hartree.

Table 5.1 shows RMS error and MAE for the occupied eigenenergies ($\{\varepsilon_i\}_{i=1}^{1024}$) and the unoccupied eigenenergies ($\{\varepsilon_i\}_{i=1026}^{1100}$) obtained from the PBE calculation. Here i is the orbital index for the total system. The absolute error for the energy level of the half filled donor state ($i = 1025$) is 0.004 eV. With the reduction scheme, the basis set size is reduced to two-third of the original basis set without compromise of the accuracy as described in Sec. 4.1.5. For the PBE0 hybrid functional, we note that RMS error and MAE for the occupied energy levels are 0.034 eV and 0.118 eV, respectively, and the absolute error for the donor state is 0.107 eV.

The binding energy of the donor state can be simply estimated from the eigenenergies: $E_b = \varepsilon_{i=1026} - \varepsilon_{i=1025}$. Table 5.2 shows E_b for P-doped Si, where we compare the results of the conventional and DC-LCFO calculations for PBE and PBE0 functionals with the experimental value. Here we also compare the band gap $E_g = \varepsilon_{i=1026} - \varepsilon_{i=1024}$ and the

43

valence-band width $W = \varepsilon_{i=1024} - \varepsilon_{i=1}$ obtained from our calculations with those of the experimental values for the bulk Si. The experimental values are taken from Ref. [52] and Ref. [54]. The PBE (PBE0) results underestimate (overestimate) these values and the difference between the conventional and DC-LCFO is not significant.

Figure 5.1 illustrates the wave function of the donor state with our method and the conventional method for comparison. Here, we show the GGA-PBE result, with the reduction scheme for DC-LCFO. Notably, the donor state with DC-LCFO agrees well with that of the conventional case.

In Fig. 5.2, the 3 highest occupied states of DC-LCFO ($\{\psi_i^{\mathrm{LCFO}}\}_{i=1022}^{1024}$) disagree with those of the conventional case ($\{\psi_i^{\mathrm{conv.}}\}_{i=1022}^{1024}$). This discrepancy comes from the hybridization of the degenerate 3 states. We perform a unitary transformation to resolve the hybridization in a similar way to Eq. (4.2), and confirm these states agree with the conventional results (see Fig. 5.2g–5.2i).

Similarly, Fig. 5.3 shows the 3 lowest unoccupied states ($i = 1026$–1028). These 3 states also degenerate and hybridize with each other. The unitary transformation yields reasonable shape of the wavefunctions (Fig. 5.3g–5.3i). From these results it can be seen that DC-LCFO can properly represent the wave function extended over fragments.

Table 5.1: RMS error and MAE (in eV) for occupied and unoccupied states of P-doped Si with the PBE functional (see the text for details of the parameters). "full" and "reduced" indicate the case with and without the reduction scheme of Sec. 3.5.2. $N_{\text{basis}}/N_{\text{atom}}$ is the number of basis functions per atom.

	RMS (occ)	MAE (occ)	RMS (unocc)	MAE (unocc)	$N_{\text{basis}}/N_{\text{atom}}$
full	0.013	0.084	0.061	0.133	17.67
reduced	0.014	0.108	0.049	0.113	10.63

Table 5.2: Binding energy of the donor state E_b for P-doped Si. We compare the results of the conventional and DC-LCFO calculations for PBE and PBE0 functionals with the experimental values. We also compare the band gap E_g and the valence-band width W obtained from our calculations with those of the experimental values for the bulk Si (in parentheses). The parameter ε_{cut} is set to $\varepsilon_{\text{cut}} - \mu = 8.163$ eV (0.3 Hartree) for PBE, and $\varepsilon_{\text{cut}} - \mu = 1.361$ eV (0.05 Hartree) for PBE0. The experimental values are taken from Ref. [52] and Ref. [54].

	Conv.(PBE)	LCFO(PBE)	Conv.(PBE0)	LCFO(PBE0)	Expt.
E_b (meV)	30.79	38.60	64.21	53.95	45.59
E_g (eV)	0.634	0.609	1.680	1.724	(1.12)
W (eV)	12.56	12.69	14.08	14.25	(12.5 ± 0.6)

(a) [0.995]　　　　　　　　(b)
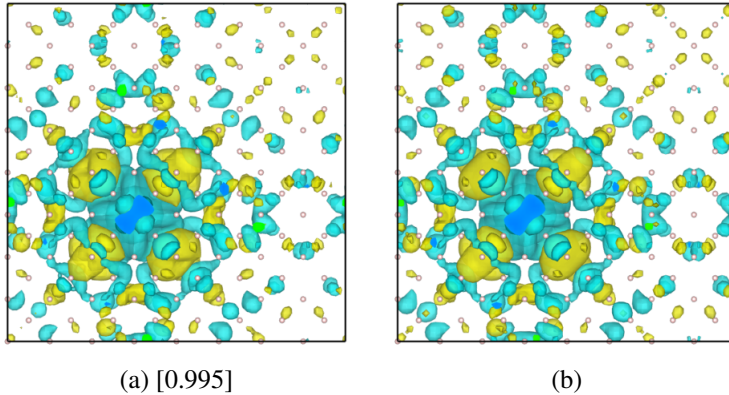
Figure 5.1: (a) DC-LCFO wave function of the donor state for the P-doped Si, with the value of the overlap with the conventional result (in square bracket). The system contains 511 Si atoms and 1 P atom in a cubic $4 \times 4 \times 4$ supercell. (b) The conventional result for comparison.
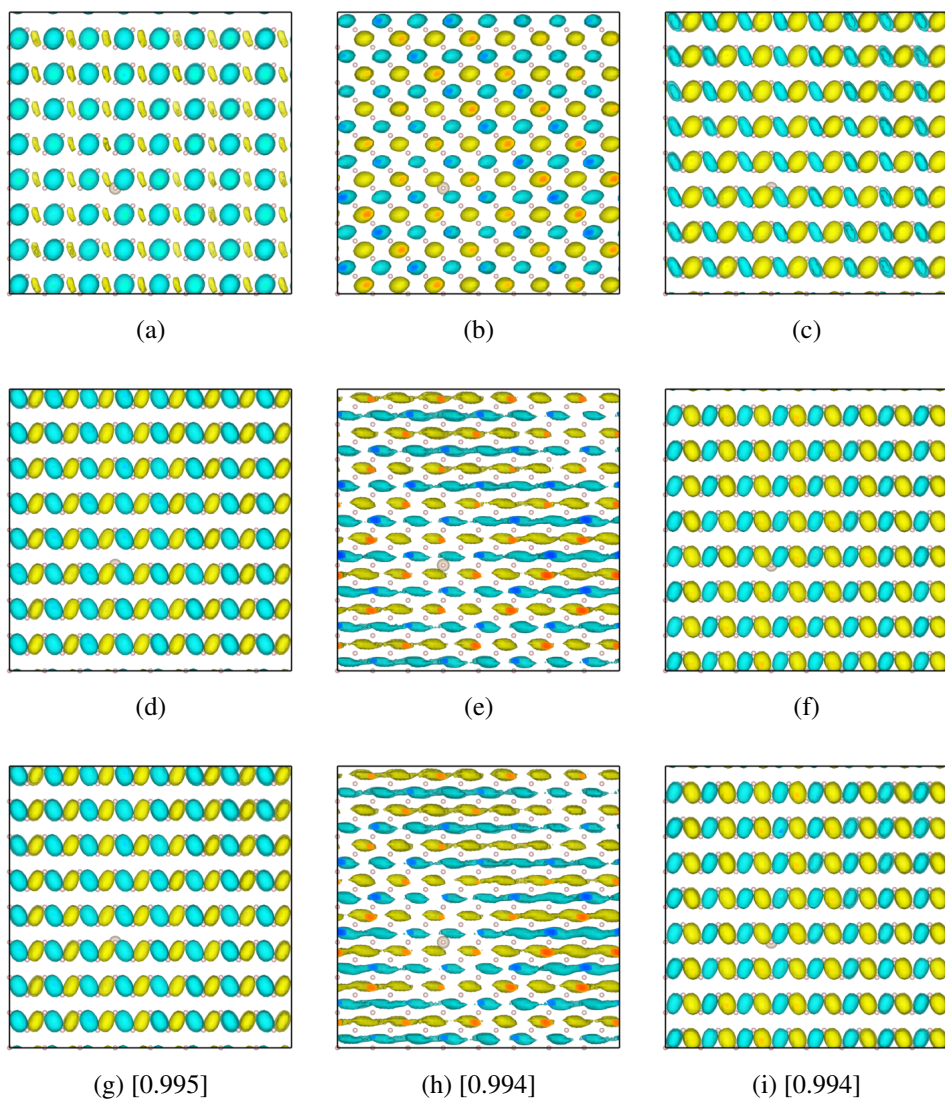
Figure 5.2: Wavefunctions of the 3 degenerate highest occupied states for P-doped Si. (a), (b) and (c) show DC-LCFO results without the unitary transformation. (d), (e) and (f) are the conventional results. (g), (h) and (i) are the unitary transformed wavefunctions of DC-LCFO, see Eq. (4.2). Here (g)–(i) are attached the value of the overlap with the corresponding conventional result (in square bracket).

(a)   (b)   (c)

(d)   (e)   (f)

(g) [0.982]   (h) [0.979]   (i) [0.989]
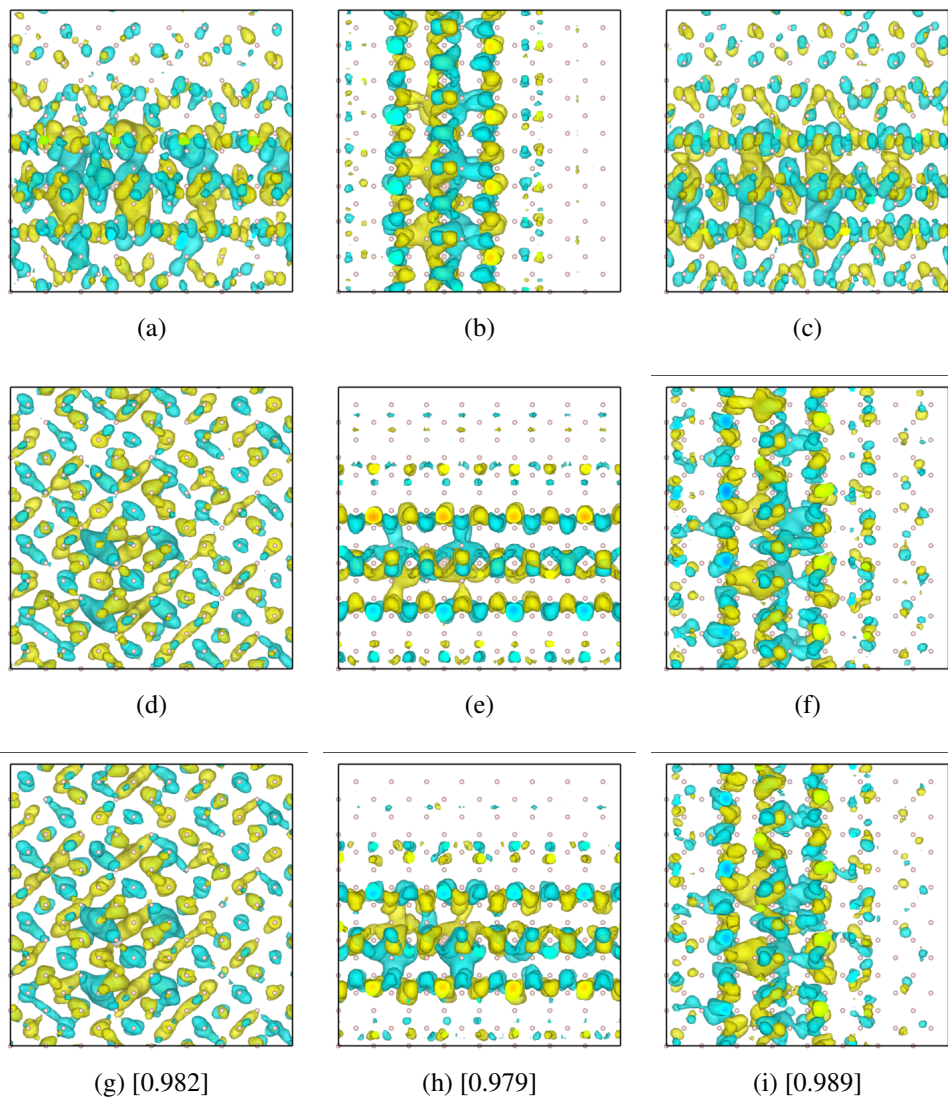
Figure 5.3: Same as Fig. 5.2, but for the 3 degenerate lowest unoccupied states for P-doped Si. (a), (b) and (c) show DC-LCFO results without the unitary transformation. (d), (e) and (f) are the conventional results. (g), (h) and (i) are the unitary transformed wave-functions of DC-LCFO, with the value of the overlap with the corresponding conventional result (in square bracket).

47

5.2 Phosphorus doped Germanium

We also perform a calculation with the PBE0 hybrid functional for a P-doped Ge crystal containing 512 atoms. The calculation conditions are almost the same for the case of Sec. 5.1. Namely, we divide the system into $4 \times 4 \times 4$ fragments and set the parameters as follows: $b' = b = a$, $\lambda_{cut} = 10^{-3}$, $\varepsilon_{cut} - \mu = 0.25$ Hartree, and $\varepsilon_{cut} - \varepsilon'_{cut} = 10^{-2.5}$ Hartree. Here, the lattice constant a is set to the experimental value 5.66 Å. The cutoff parameter for the exact exchange potential R_c is set to 8 a.u. $= 4.23$ Å $< b'$. The plane-wave cutoff is 32.5 Ry and the number of the FFT mesh points is equal to $20 \times 20 \times 20$ in each core domain.

RMS error and MAE for the occupied eigenenergies are 0.025 eV and 0.127 eV, respectively, and the absolute error for the donor state is 0.062 eV.

Table 5.3 shows the binding energy of the donor state E_b, band gap E_g, and valence-band width W. While our calculations overestimate these value due to the nature of the PBE0 functional, the difference between the conventional and DC-LCFO is not significant.

Figuer 5.4 illustrates the wavefunction of the donor state. We see that our method reproduces well the spatially extended state in a similar way to the case of P-doped Si.

Table 5.3: Binding energy of the donor state E_b, band gap E_g, and valence-band width W for P-doped Ge. We compare the results of the conventional and DC-LCFO calculations for the PBE0 functional with the experimental values, where E_g and W are the values for the bulk Ge (in parentheses). The experimental values are taken from Ref. [52] and Ref. [54].

	Conv.	LCFO	Expt.
E_b (meV)	103.8	66.58	12.88
E_g (eV)	1.455	1.354	(0.66)
W (eV)	14.07	14.19	(12.9 ± 0.2)

(a) [0.973]   (b)
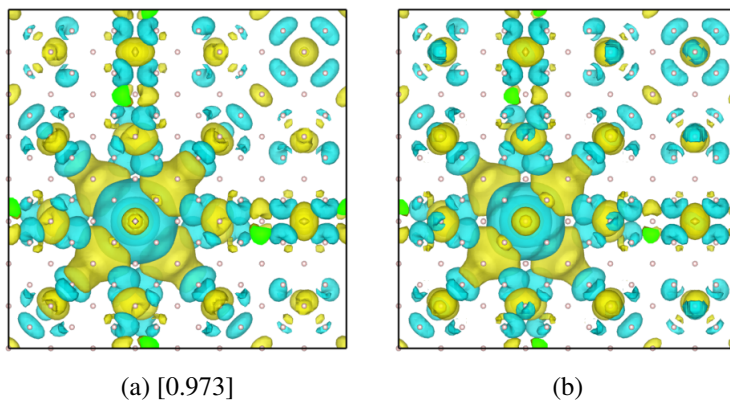
Figure 5.4: (a) DC-LCFO wave function of the donor state for the P-doped Ge, with the value of the overlap with the conventional result (in square bracket). The system contains 511 Ge atoms and 1 P atom in a cubic $4 \times 4 \times 4$ supercell. (b) The conventional result for comparison.

5.3 InGaN/GaN superlattice

We applied our method to a superlattice system with the band-bending structure. The heterostructures of the wurtzite III-V nitrides with [0001] epitaxial alignments have the polar interface which induces the band bending [55, 56]. This polarization is due to the low-symmetry structure of the wurtzite III-V nitrides [55]. Here we focus on the In-GaN/GaN superlattice [57], which has many practical applications in devices such as the light emitting diode (LED).

We shall show results of the eigenstates calculation for $(In_{0.5}Ga_{0.5}N)_{24}/(GaN)_{24}$ super-lattice which contains 768 atoms in a rectangular cell of side lengths, $12.89 \times 5.58 \times 131.06$ (in Å). The structure of each GaN or InGaN layer is depicted in Fig. 5.5. The lattice parameters in the x-y plane (orthogonal to [0001] direction) are set to those of the bulk GaN, whereas, the lattice parameters along z ([0001]) direction for GaN and InGaN are set to 5.239 Å and 5.683 Å, respectively, which are determined by the strain condition (Sec. II of Ref. [57]). Here, we utilize the unoptimized crystal structure since we are only interested in calculation of the electronic state.

The system is divided into 12 fragments with 1D ($1 \times 1 \times 12$) configurations. The buffer thickness b is equal to the length of each core domain along the z direction, while the x-y plane is not divided so $b = 0$ in the x-y plane. The electron temperature is set to 316 K (= 0.001 Hartree/k_B). The parameters for the eigenstate calculation are fixed as $b' = b$, $\lambda_{cut} = 10^{-3}$, and $\varepsilon_{cut} - \mu = 8.163$ eV (0.3 Hartree). The parameter for the reduction scheme is set as $\varepsilon_{cut} - \varepsilon'_{cut} = 10^{-2.5}$ Hartree. The plane-wave cutoff is 50 Ry and the number of the FFT mesh points is equal to $60 \times 24 \times 48$ in each core domain.

Table 5.4 shows the RMS error and MAE for the occupied eigenenergies ($\{\varepsilon_i\}_{i=1}^{1536}$) and the unoccupied eigenenergies ($\{\varepsilon_i\}_{i=1537}^{1700}$). The number of the basis functions is extremely small even before performing the reduction. The reduction scheme yields no substantial effect and these small basis sets give sufficient accuracy because of the 1D configuration of the fragments where each fragment has only two buffer regions in contrast to 26 in case of 3D configuration. We can deduce that the unphysical zero eigenvalues (Sec. 3.5) originate from the buffer regions.

Figure 5.6 shows the local density of states (LDOS) with our method and the conventional method, where the [0001] axis coincides with the horizontal direction of the text. This result demonstrates that our method can reproduce a large-scale band structure such as the band bending in good agreement with conventional calculations.
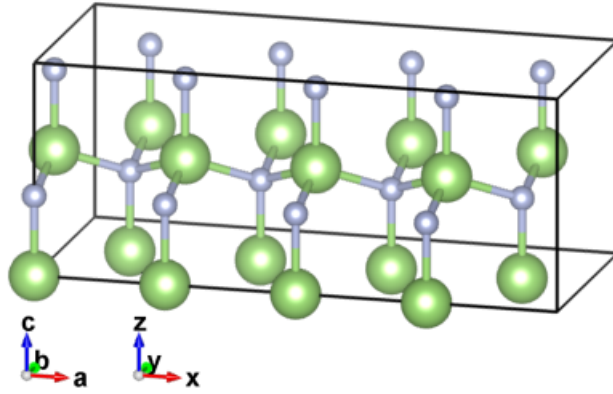
Figure 5.5: Wurtzite unit cell containing 2 GaN layers, 32 atoms. [0001] direction coincides z axis.

Table 5.4: RMS error and MAE (in eV) for occupied and unoccupied states of In-GaN/GaN superlattice (see the text). "full" and "reduced" indicate the case with and without the reduction scheme of Sec. 3.5.2. N_{basis}/N_{atom} is the number of basis functions per atom.

	RMS (occ)	MAE (occ)	RMS (unocc)	MAE (unocc)	N_{basis}/N_{atom}
full	0.031	0.186	0.027	0.084	4.30
reduced	0.030	0.181	0.027	0.081	3.66
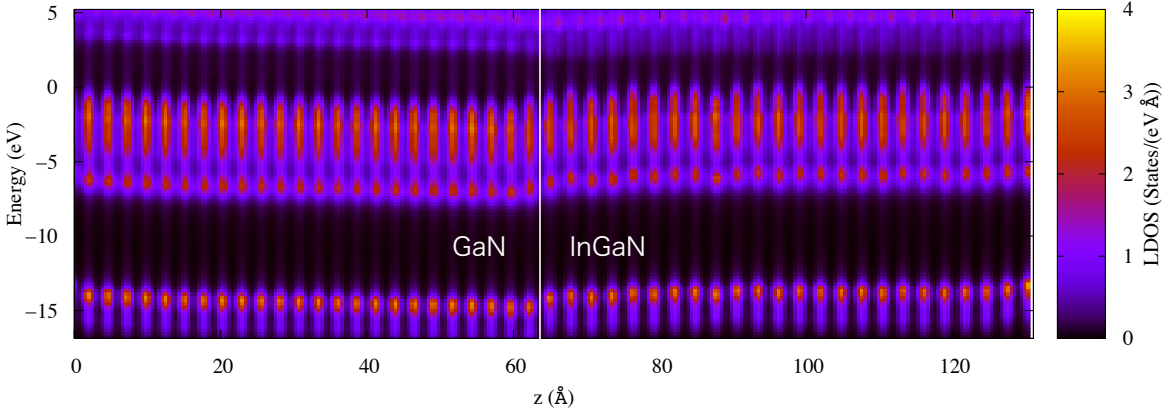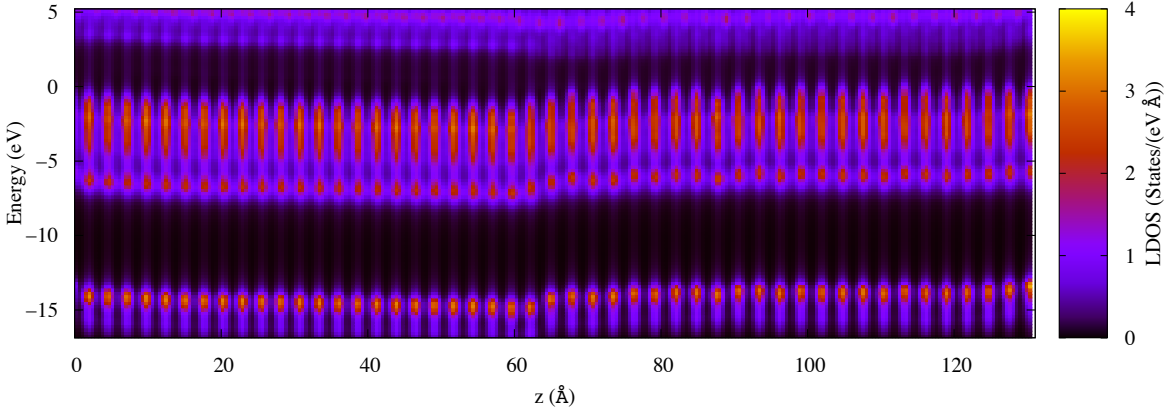
Figure 5.6: (a) DC-LCFO result of the local density of states (LDOS) for the InGaN/GaN superlattice system, which is composed of 24 InGaN layers and 24 GaN layers, where each layer contains 16 atoms. The system is divided into 12 fragments along the z-direction. (b) The conventional result for comparison.

Chapter 6

Conclusion

In this thesis, we developed a method for accelerating the electronic structure calculations within the divide-and-conquer (DC) approach to DFT. The method is shown to allow us to efficiently calculate the wavefunctions (Kohn-Sham orbitals) although the DC-DFT has been incapable of doing this in general. This study was motivated by the fact that the conventional first-principles electronic structure calculations using the semi-local density functionals have been seriously bottlenecked by the $O(N_{\mathrm{basis}}^3)$ scaling versus the basis-set size N_{basis}. The situation is made more serious when performing more accurate first-principles calculations using numerically demanding non-local operators, such as the exact exchange potential. In this context, FMO-LCMO was previously developed on the basis of DC approach. In this method, however, the whole system is decomposed into non-overlapping fragments by cutting the covalent bond, so that it is applicable only to covalently bonded systems like biological molecules. This problem can be overcome by decomposing the whole space into overlapping fragments; however, the decomposition becomes less unambiguous and, moreover, method to handle buffer regions (overlap regions) of the fragments has been unknown thus far. To overcome this problem, we developed a scheme to manage the overlapping fragments by properly removing or utilizing information of the buffer regions depending on the objective.

The key of the formulation is in the construction of the basis functions and in the calculation of the Hamiltonian matrix elements. The basis function is derived from the orbitals of the respective fragments including the buffer region, but buffer's contribution is spatially removed: In doing so, it is crucially important to remove the linearly dependent functions. By this procedure, the basis-set size is significantly reduced. In addition, the Hamiltonian matrix elements can be partitioned into parts, which can be calculated at each fragment independently from others. The inter-fragment (off-diagonal) elements of the Hamiltonian matrix are represented by the orbitals of the corresponding fragment including the buffer region. The remaining task is to calculate the inner products among the fragment orbitals, but the calculation is not so time-consuming.

The construction of the basis set and the Hamiltonian matrix can be performed with $O(N)$ cost. Also, the diagonalization of the Hamiltonian matrix requires modest $O(N_{\mathrm{basis}}^3)$ cost thanks to the small matrix dimension N_{basis}. In addition, the scaling of the computational cost is the same whether or not using the numerically demanding non-local

operators within each fragment. This means that, calculations with the exact exchange potential is greatly facilitated by our method. Thus we have established a high-speed and versatile computation method for electronic states.

We have examined specific conditions for achieving reliable results and demonstrated efficiency of our method. While we used LDC-DFT as the basis of our research, our novel basis set and Hamiltonian construction method can be applied to general DC approaches. This study paves the way for large-scale electronic state calculations in a broad class of research fields.

In Chapter 2, we reviewed the fundamental formulation of DFT and DC-DFT. We also mentioned the nearsighted principle for electronic matter, which is the physical basis of the DC approach.

In Chapter 3, we presented the formalism of our method. We explained the detailed procedure for the construction of the basis functions and the Hamiltonian matrix, and discussed the advantages of our method. Moreover, we mentioned the existence of the unphysical zero eigenvalues originating from the buffer regions, and proposed the technique for further reduction of the basis-set size in which the unphysical eigenvectors are eliminated with a simple algorithm.

In Chapter 4, we investigated the parameter dependence of our method and performed the benchmark test. The former results revealed reasonable parameter conditions. In particular, the buffer thickness b' (truncation range of the Hamiltonian operator) is not required to optimize and is uniquely determined as $b' = b$ (buffer thickness of the DC calculation). This implies a hidden advantage of LDC-DFT: the periodic boundary conditions imposed at the fragment boundary alleviate the drawback by the artificial boundaries. We also referred to the other parameters controlling the accuracy and their tradeoff relation between the accuracy and the computational cost. In the benchmark test, we showed that our method can substantially reduce the computational time for the Hamiltonian construction and diagonalization, regardless of the inclusion of the exact exchange potential.

In Chapter 5, we applied our method to the defect structure and the superlattice structure with the band bending. For P-doped Si crystal, we performed the calculations with the GGA exchange-correlation functional and the hybrid functional. We compared the binding energy, the band gap, and the valence band width obtained from these calculations with those of the experimental values. We also performed the PBE0 calculation for P-doped Ge crystal, where the conventional LDA and GGA calculations incorrectly yield metallic state. For InGaN/GaN superlattice, we confirmed that our method can represent the global band structure such as the band bending. With these results, we found that the number of the basis functions per atom can be reduced down to roughly 4–10 depending on configurations of the fragments with keeping practical accuracy. Actually, it seems that the size of the buffer region around the core domain determines the basis set size. This indicates the unphysical eigenvectors within the Hamiltonian matrix originate from the buffer regions. The complete removal of the remaining unphysical eigenvectors is a problem left for the future.

We conclude this thesis by making some remarks on future prospects of the present method. Our method is a powerful tool for studying the nature of electronic states for large

systems. Particularly, the electronic state calculations for general disordered materials can be much facilitated by our method thanks to their short correlation length. While ordered metallic systems require large buffer regions due to their long correlation length, our method can be in principles applicable.

With the universality of DC approach, the present method offers many possibilities of application to various fields. For example, our scheme can be extended to more general Hamiltonians including short-range exchange-correlation terms such as the GW self-energy operator [58–60] in principle. The other possibility is an extension to the time-dependent density functional theory (TD-DFT). There is a method for facilitating the TD-DFT calculation by employing the static KS orbitals of subsystems as a basis set [61], which is related to the Green's function method referred to in the last of Sec. 3.1. Ref. [62] has showed that a basis set consists of the occupied and few unoccupied KS orbitals and the occupied orbitals with the shifted k points yields the high-speed TD-DFT calculation thanks to the small basis-set size. Our Hamiltonian construction based on the fragment electronic states is obviously applicable to these methods, which could provide a new real-time method for TD-DFT with our basis set.

Appendix A

Comparison with FMO-LCMO
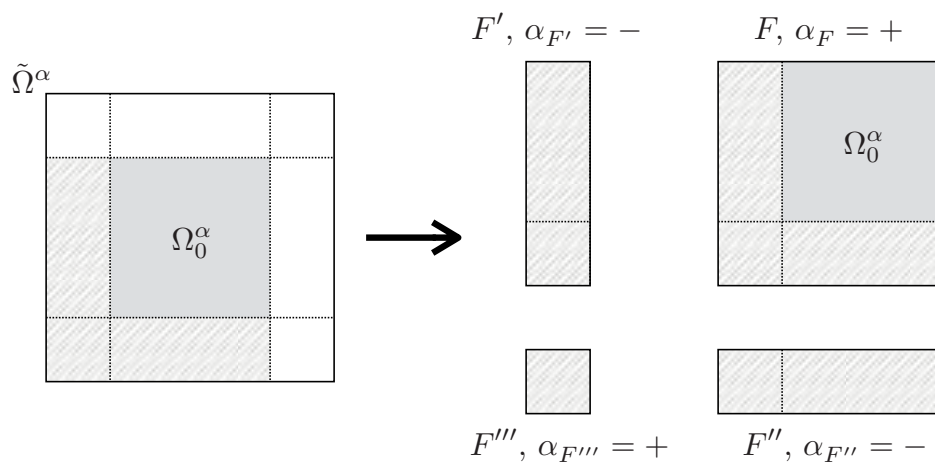
Figure A.1: LS3DF-like decomposition of the fragment Hamiltonian $\hat{H}^\alpha$. Compare with Fig. 2.4.

In Sec. 3.3, we formulated the approximate expression for the Hamiltonian matrix, starting from the consideration of the Hamiltonian operation on the basis functions. In FMO-LCMO, on the other hand, the approximate Hamiltonian is represented as a decomposed operator which consists of the fragment Hamiltonian operators. Let us discuss the relation between these two formulations.

FMO-LCMO applies the FMO summation formula Eq. (2.23) to the Hamiltonian operator. Namely, the total Hamiltonian is decomposed into the fragment monomer and

fragment dimer terms as follows [40, 41]:

$$\hat{H} = \sum_I \hat{H}_I + \sum_{I>J} \left(\hat{H}_{IJ} - \hat{H}_I - \hat{H}_J \right), \tag{A.1}$$

where we omit the higher terms such as the fragment trimer (FMO2 level). I and J are indices of the fragment monomers and $\hat{H}_I$ denotes the Hamiltonian for the fragment monomer I. $\hat{H}_{IJ}$ represents the Hamiltonian for the fragment dimer IJ. The second term represents the non-local effects across the monomers, while the first term indicates the monomer effects.

One can construct a representation analogous to Eq. (A.1) for the Hamiltonian operator so that its matrix elements agree with Eq. (3.11). This representation is formulated by the summation of the fragment Hamiltonians in a similar way to the density summation formula Eq. (2.24) of LS3DF. For simplicity, we consider only a case of 2D systems. Here, each $\tilde{\Omega}^\alpha$ is divided into 4 small fragments and they are assigned new indices F. For each fragment F, we assign a sign factor $\alpha_F = \pm$ depending on the layout of the fragment (Fig. A.1). The approximated Hamiltonian operator of the whole system can be expressed as,

$$\hat{H}_{\text{approx.}} = \sum_F \alpha_F \hat{H}_F, \tag{A.2}$$

where $\hat{H}_F = \hat{P}^F \hat{H}^\alpha \hat{P}^F$ is a projected Hamiltonian for the small fragment F.

With the above $\hat{H}_{\text{approx.}}$, the matrix elements are completely identical to $\langle \lambda_{i'}^{\alpha'} | \hat{P}^\beta \hat{H}^\beta \hat{P}^\beta | \lambda_i^\alpha \rangle$ with a proper configuration of the fragment β. Specifically, we put $\beta = \alpha$ (α') if the fragment α is located at the north/north-east/east (south/south-west/west) of the fragment α' in 2D systems, while β indicates the other fragment overlapping with both α and α' if the fragment α is located at the north-west/south-east of the fragment α' as Fig. 3.2b.

Appendix B

k-point sampling with DC-LCFO

DC-LCFO gives us eigenstates corresponding to the Γ point in the Brillouin zone. However, the energy band calculations for a large system is often required. For example, Ref. [33] utilized an energy band of 13468-atom supercell (Fig. 3c in Ref. [33]) to investigate properties of the Dirac electron in the twisted bilayer graphene.

In this appendix, we describe an extension of DC-LCFO for calculating the eigenstates with the k-point sampling. We shall start with a review for the Bloch states. In Sec. B.2, we will present a method for calculating the Hamiltonian matrix elements for the Bloch states using the basis set derived from DC-LCFO. This argument explains why DC-LCFO could generate the eigenenergies of $N \times 1 \times 1$ cell (N =12, 27, 54) from the wavefunctions of $3 \times 1 \times 1$ in Sec. 4.2.

B.1   Hamiltonian matrix for Bloch states

For simplicity, we consider a 1-dimensional periodic system with the size of $L = N_k a$, where N_k is a integer and a is a period of the Hamiltonian. The plane waves $\{|k\rangle\}$ are defined as

$$\langle x|k \rangle = e^{ikx}/\sqrt{L}, \quad k = 2\pi n/L \, (n \in \mathbb{Z}). \tag{B.1}$$

The Hamiltonian is written as

$$\hat{H} = -\frac{1}{2}\frac{\partial^2}{\partial x^2} + V(\hat{x}), \quad V(x) = \sum_G V(G)e^{iGx}, \tag{B.2}$$

where $G = 2\pi n/a \, (n \in \mathbb{Z})$ is the reciprocal lattice vector corresponding to the periodicity $V(x + a) = V(x)$.

The N_k Bloch states are given as follows:

$$|\psi_{kn}\rangle = \sum_G C_{kn}(G)|k + G\rangle, \tag{B.3}$$

where $k = 2\pi n/L \, (n = 0, 1, \cdots, N_k - 1)$ means the independent k-vector in the Brillouin

zone, and C_{kn} is the expansion coefficient. These wavefunctions can be rewritten as

$$|\psi_{kn}\rangle = e^{ik\hat{x}}|u_{kn}\rangle, \quad |u_{kn}\rangle = \sum_G C_{kn}(G)|G\rangle, \tag{B.4}$$

where $u_{kn}(x)$ is the periodic function: $u_{kn}(x + a) = u_{kn}(x)$. Thus the Bloch states at each k-point can be obtained by diagonalizing the Hamiltonian $e^{-ik\hat{x}}\hat{H}e^{ik\hat{x}}$ with periodic basis functions $\{|\chi_i\rangle\}$: $\chi_i(x + a) = \chi_i(x)$.

B.2 Bloch states in DC-LCFO

Let us consider that $[0, a]$ is divided into n_f fragments. Each core domain Ω_0^α is equal to $[(\alpha - 1)\frac{a}{n_f}, \alpha\frac{a}{n_f}]$, where $\alpha = 1, \cdots, n_f$. If a is sufficiently large such that the non-local terms of the Hamiltonian have no double counting by periodicity, the Hamiltonian in the supercell $[0, a]$ can be obtained by DC-LCFO. Namely,

$$\hat{H}_{[0,a]} = \sum_{\alpha'=1}^{n_f} \sum_{j'=1}^{M_{\alpha'}} \sum_{\alpha=1}^{n_f} \sum_{j=1}^{M_\alpha} |\lambda_{j'}^{\alpha'}\rangle H_{\alpha'j',\alpha j}\langle\lambda_j^\alpha|, \tag{B.5}$$

where the off-diagonal block $\{H_{n_f,j';1,j}\}$ is nonzero due to the periodicity at $x = 0$ and $x = a$.

We can obtain the Bloch states at the k-point by simply diagonalizing the matrix

$$H_{\alpha'j',\alpha j}(k) = \langle\lambda_{j'}^{\alpha'}|e^{-ik\hat{x}}\hat{H}_{[0,a]}e^{ik\hat{x}}|\lambda_j^\alpha\rangle\exp\left(ika\,\delta_{n_f-1,|\alpha'-\alpha|}\frac{\alpha'-\alpha}{n_f-1}\right). \tag{B.6}$$

Here, the integration interval for the inner product is $[0, a]$. The phase factor $\exp(\cdots)$ becomes e^{ika} (e^{-ika}) if $\alpha' = n_f$ and $\alpha = 1$ ($\alpha' = 1$ and $\alpha = n_f$), and $\exp(\cdots) = 1$ for otherwise. Needless to say, the case of $k = 0$ corresponds to the DC-LCFO calculation.

This expression can be justified as follows: Let us enlarge the cell $[0, a]$ to $[0, N_k a]$. With the translation operator $\hat{T} \equiv \exp(-ia\hat{p}) = \exp(-a\frac{\partial}{\partial x})$, we can construct a basis set for the enlarged cell from $\{|\lambda_j^\alpha\rangle\}$,

$$\{|\lambda^\alpha\rangle, \hat{T}|\lambda^\alpha\rangle, \hat{T}^2|\lambda^\alpha\rangle, \cdots, \hat{T}^{N_k-1}|\lambda^\alpha\rangle\}, \tag{B.7}$$

where we omit the orbital index j for brevity. The Hamiltonian for $[0, N_k a]$ is defined as

$$\hat{H} = \sum_{\alpha',\alpha=1}^{n_f} \sum_{m',m=0}^{N_k-1} \hat{T}^{m'}|\lambda^{\alpha'}\rangle H'_{m'\alpha';m\alpha}\langle\lambda^\alpha|\hat{T}^{m\dagger}, \tag{B.8}$$

where $H'_{m'\alpha';m\alpha}$ is equal to the corresponding $H_{\alpha',\alpha}$, which is given in Eq. (B.5), for the basis functions at the same or neighboring positions. Here, we put $H'_{m-1,n_f;m,1} = H_{n_f,1}$ and $H'_{m,n_f;m,1} = 0$ with the consideration of the periodicity. This Hamiltonian construction is analogous to that of Sec. 4.2 with $n_f = 1$ and $N_k = N$ ($N = 12, 27, 54$).

The periodic basis functions can be obtained as

$$|\chi_\alpha\rangle = \frac{1}{\sqrt{N_k}} \sum_{m=0}^{N_k-1} \hat{T}^m |\lambda^\alpha\rangle. \tag{B.9}$$

Using this basis set, we can describe the matrix elements of $e^{-ik\hat{x}} \hat{H} e^{ik\hat{x}}$ as

$$
\begin{aligned}
\langle \chi_{\alpha'} | e^{-ik\hat{x}} \hat{H} e^{ik\hat{x}} | \chi_\alpha \rangle &= \frac{1}{N_k} \sum_{m\,m'm_1 m_2} \sum_{\alpha_1 \alpha_2} \langle \lambda^{\alpha'} | \hat{T}^{m'\dagger} e^{-ik\hat{x}} \hat{T}^{m_1} | \lambda^{\alpha_1} \rangle H'_{m_1\alpha_1; m_2\alpha_2} \langle \lambda^{\alpha_2} | \hat{T}^{m_2\dagger} e^{ik\hat{x}} \hat{T}^m | \lambda^\alpha \rangle \\
&= \frac{1}{N_k} \sum_{m'm} \langle \lambda^{\alpha'} | \hat{T}^{m'\dagger} e^{-ik\hat{x}} \hat{T}^{m'} | \lambda^{\alpha'} \rangle H'_{m'\alpha'; m\alpha} \langle \lambda^\alpha | \hat{T}^{m\dagger} e^{ik\hat{x}} \hat{T}^m | \lambda^\alpha \rangle \\
&= \frac{1}{N_k} \sum_{m'm} H'_{m'\alpha'; m\alpha} e^{-ika(m'-m)} \langle \lambda^{\alpha'} | e^{-ik\hat{x}} | \lambda^{\alpha'} \rangle \langle \lambda^\alpha | e^{ik\hat{x}} | \lambda^\alpha \rangle, \tag{B.10}
\end{aligned}
$$

where we used $\hat{T}^{m\dagger} e^{ik\hat{x}} \hat{T}^m = e^{imka} e^{ik\hat{x}}$. In the case of that $H'_{m'\alpha'; m\alpha}$ has a nonzero value if and only if $m' = m$,

$$(\text{B.10}) = \frac{1}{N_k} H_{\alpha',\alpha} N_k \langle \lambda^{\alpha'} | e^{-ik\hat{x}} | \lambda^{\alpha'} \rangle \langle \lambda^\alpha | e^{ik\hat{x}} | \lambda^\alpha \rangle, \tag{B.11}$$

and this agrees with Eq. (B.6). In the case of that $\alpha' = n_f$ and $\alpha = 1$, then $m' = m - 1$, the matrix element can be rewritten as

$$(\text{B.10}) = e^{ika} H_{n_f,1} \langle \lambda^{n_f} | e^{-ik\hat{x}} | \lambda^{n_f} \rangle \langle \lambda^1 | e^{ik\hat{x}} | \lambda^1 \rangle, \tag{B.12}$$

and identical to Eq. (B.6). The phase factor e^{ika} cannot be removed due to the periodicity of the system.

Bibliography

[1] P. Hohenberg and W. Kohn. *Phys. Rev.*, 136:B864, 1964.

[2] W. Kohn and L. J. Sham. *Phys. Rev.*, 140:A1133, 1965.

[3] D. R. Bowler and T. Miyazaki. *Rep. Prog. Phys.*, 75:036503, 2012.

[4] S. Goedecker. *Rev. Mod. Phys.*, 71:1085, 1999.

[5] T. L. Beck. *Rev. Mod. Phys.*, 72:1041, 2000.

[6] T. Torsti, T. Eirola, J. Enkovaara, T. Hakala, P. Havu, V. Havu, T. Höynälänmaa, J. Ignatius, M. Lyly, I. Makkonen, T. T. Rantala, J. Ruokolainen, K. Ruotsalainen, E. Räsänen, H. Saarikoski, and M. J. Puska. *phys. stat. sol.*, 243:1016, 2006.

[7] Y. Saad, J.R. Chelikowsky, and S. M. Shontz. *SIAM Review*, 52:3, 2010.

[8] J. E. Pask and P. A. Sterne. *Model. Sim. Mat. Sci. Eng.*, 13:R71, 2005.

[9] L. Genovese, A. Neelov, S. Goedecker, T. Deutsch, S. Ghasemi, A. Willand, D. Caliste, O. Zilberberg, M. Rayson, A. Bergman, and R. Schneider. *J. Chem. Phys.*, 129:014109, 2008.

[10] K. Varga, Z. Zhang, and S. T. Pantelides. *Phys. Rev. Lett.*, 93:176403, 2004.

[11] J. Bernholc, M. Hodak, and W. Lu. *J. Phys.: Condens. Matter*, 20:294205, 2008.

[12] H. Shang, H. Xiang, Z. Li, and J. Yang. *Int. Rev. Phys. Chem.*, 29:665, 2010.

[13] J. M. Soler, E. Artacho, J. D. Gale, A. García, J. Junquera, P. Ordejón, and D. Sánchez-Portal. *J. Phys.: Condens. Matter*, 14:2745, 2002.

[14] S. Ismail-Beigi and T. A. Arias. *Phys. Rev. Lett.*, 82:2127, 1999.

[15] E. H. Rubensson and E. Rudberg. *J. Comput. Chem.*, 32:1411, 2011.

[16] W. Kohn. *Int. J. Quantum Chem.*, 56:229, 1995.

[17] R. Haydock, V. Heine, and M. J. Kelly. *J. Phys. C*, 5:2845, 1972.

[18] R. Haydock. *Solid State Phys.*, 35:216, 1980.

[19] T. Ozaki, M. Aoki, and D. G. Pettifor. *Phys. Rev. B*, 61:7972, 2000.

[20] T. Ozaki. *Phys. Rev. B*, 74:245101, 2006.

[21] R. Takayama, T. Hoshi, and T. Fujiwara. *J. Phys. Soc. Jpn*, 73:1519, 2004.

[22] K. Varga. *Phys. Rev. B*, 81:045109, 2010.

[23] W. T. Yang. *Phys. Rev. Lett.*, 66:1438, 1991.

[24] S. L. Dixon and K. M. Merz. *J. Chem. Phys.*, 107:879, 1997.

[25] F. Shimojo, R. K. Kalia, A. Nakano, and P. Vashishta. *Comput. Phys. Commun.*, 167:151, 2005.

[26] M. Kobayashi and H. Nakai. *J. Chem. Phys.*, 129:044103, 2008.

[27] F. Shimojo, R. K. Kalia, A. Nakano, and P. Vashishta. *Phys. Rev. B*, 77:085103, 2008.

[28] L. W. Wang, Z. Zhao, and J. C. Meza. *Phys. Rev. B*, 77:165113, 2008.

[29] Z. Zhao, L. W. Wang, and J. C. Meza. *J. Phys.: Condens. Matter*, 20:294203, 2008.

[30] N. Ohba, S. Ogata, T. Kouno, T. Tanmura, and R. Kobayashi. *Comput. Phys. Commun.*, 183:1664, 2012.

[31] F. Shimojo, S. Hattori, R.K. Kalia, M. Kunaseth, W. Mou, A. Nakano, K. Nomura, S. Ohmura, P. Rajak, K. Shimamura, and P. Vashishta. *J. Chem. Phys.*, 140:18A529, 2014.

[32] J. Iwata, D. Takahashi, A. Oshiyama, T. Boku, K. Shiraishi, S. Okada, and K. Yabana. *J. Comput. Phys.*, 229:2339, 2010.

[33] K. Uchida, S. Furuya, J. Iwata, and A. Oshiyama. *Phys. Rev. B*, 90:155451, 2014.

[34] A. Nakata, D. R. Bowler, and T. Miyazaki. *J. Chem. Theory Comput.*, 10:4813, 2014.

[35] A. Nakata, D. R. Bowler, and T. Miyazaki. *Phys. Chem. Chem. Phys.*, 17:31427, 2015.

[36] K. Kitaura, E. Ikeo, T. Asada, T. Nakano, and M. Uebayasi. *Chem. Phys. Lett.*, 313:701, 1999.

[37] Y. Inadomi, T. Nakano, K. Kitaura, and U. Nagashima. *Chem. Phys. Lett.*, 364:139, 2002.

[38] T. Watanabe, Y. Inadomi, H. Umeda, K. Fukuzawa, S. Tanaka, T. Nakano, and U. Nagashima. *J. Comput. Theor. Nanosci.*, 6:1328, 2009.

[39] D. G. Fedorov and K. Kitaura. *J. Chem. Phys.*, 131:171106, 2009.

[40] S. Tsuneyuki, T. Kobori, K. Akagi, K. Sodeyama, K. Terakura, and H. Fukuyama. *Chem. Phys. Lett.*, 476:104, 2009.

[41] T. Kobori, K. Sodeyama, T. Otsuka, Y. Tateyama, and S. Tsuneyuki. *J. Chem. Phys.*, 139:094113, 2013.

[42] J. P. Perdew and A. Zunger. *Phys. Rev. B*, 23:5048, 1981.

[43] J. P. Perdew, K. Burke, and M. Ernzerhof. *Phys. Rev. Lett.*, 77:3865, 1996.

[44] J. P. Perdew, M. Ernzerhof, and K. Burke. *J. Chem. Phys.*, 105:9982, 1996.

[45] N. D. Mermin. *Phys. Rev.*, 137:A1441, 1965.

[46] E. Prodan and W. Kohn. *Proc. Natl. Acad. Sci. U.S.A.*, 102:11635, 2005.

[47] W. Kohn. *Phys. Rev. Lett.*, 76:3168, 1996.

[48] S. Yamada, F. Shimojo, R. Akashi, and S. Tsuneyuki. *Phys. Rev. B*, 95:045106, 2017.

[49] `http://xtapp.cp.is.s.u-tokyo.ac.jp/`. xTAPP official website (in Japanese).

[50] D. G. Anderson. *J. Assoc. Computing Machinery*, 12:547, 1965.

[51] J. Spencer and A. Alavi. *Phys. Rev. B*, 77:193110, 2008.

[52] Y. Matsushita, K. Nakamura, and A. Oshiyama. *Phys. Rev. B*, 84:075205, 2011.

[53] K. Momma and F. Izumi. *J. Appl. Cryst.*, 44:1272, 2011.

[54] A. K. Ramdas and S. Rodriguez. *Rep. Prog. Phys.*, 44:1297, 1981.

[55] F. Bernardini, V. Fiorentini, and D. Vanderbilt. *Phys. Rev. B*, 56:R10024, 1997.

[56] F. Bernardini and V. Fiorentini. *Phys. Rev. B*, 57:R9427, 1998.

[57] L. Dong, J. V. Mantese, V. Avrutin, Ü. Özgür, H. Morkoç, and S. P. Alpay. *J. Appl. Phys.*, 114:043715, 2013.

[58] L. Hedin. *Phys. Rev.*, 139:A796, 1965.

[59] L. Hedin and S. Lundqvist. *Solid State Phys.*, 23:1, 1969.

[60] M. S. Hybertsen and S. G. Louie. *Phys. Rev. Lett.*, 55:1418, 1985.

[61] V. A. Goncharov and K. Varga. *Phys. Rev. B*, 83:035118, 2011.

[62] S. A. Sato and K. Yabana. *Phys. Rev. B*, 89:224305, 2014.